Journal Pre-proofs

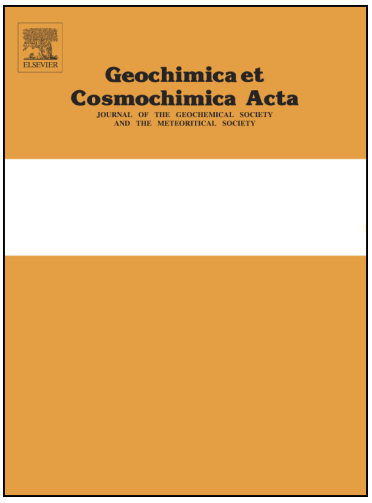

First-principles calculation of iron and silicon isotope fractionation between Fe-bearing minerals at magmatic temperatures: The importance of second atomic neighbors

S. Rabin, M. Blanchard, C. Pinilla, F. Poitrasson, M. Gregoire

PII: S0016-7037(21)00202-7
DOI: https://doi.org/10.1016/j.gca.2021.03.028
Reference: GCA 12142

To appear in: *Geochimica et Cosmochimica Acta*

Received Date: 17 July 2020
Revised Date: 17 March 2021
Accepted Date: 29 March 2021

Please cite this article as: Rabin, S., Blanchard, M., Pinilla, C., Poitrasson, F., Gregoire, M., First-principles calculation of iron and silicon isotope fractionation between Fe-bearing minerals at magmatic temperatures: The importance of second atomic neighbors, *Geochimica et Cosmochimica Acta* (2021), doi: https://doi.org/10.1016/j.gca.2021.03.028

First-principles calculation of iron and silicon isotope fractionation between Fe-bearing minerals at magmatic temperatures: The importance of second atomic neighbors

S. RABIN[1], M. BLANCHARD[1], C. PINILLA[2], F. POITRASSON[1], M. GREGOIRE[1]

[1]Laboratoire Géosciences Environnement Toulouse, CNRS-UMR5563 CNES-UPS-IRD, 14 av. E. Belin, 31400 Toulouse, France (segolene.rabin@get.omp.eu)

[2] Departamento de Fisica y Geociencias, Universidad del Norte, Barranquilla, Colombia

ABSTRACT

In order to elucidate the processes involved in iron and silicon isotopes partitioning during magmatic differentiation, it is essential to know the precise value of equilibrium fractionation factors between the main minerals present in the evolving silicic melts. In this study, we performed first-principles calculations based on the density functional theory to determine the equilibrium iron and silicon isotopes fractionation factors between eleven relevant silicate or oxide minerals in the context of magmatic differentiation, namely: aegirine, hedenbergite, augite, diospide, enstatite, fayalite, hortonolite, Fe-rich and Fe-free forsterites, magnetite and ulvospinel. Results show that Fe^{2+}-bearing silicate minerals display significant differences in iron isotope fractionation factors that cannot be neglected, even at high temperature (1000°C). Various physical and chemical parameters control the iron isotopic fractionation of silicate minerals. However, the main parameter, after temperature and the iron oxidation state, is the nature and number of iron second neighbors (i.e. the local chemical composition around Fe atoms). This conclusion is also valid for silicon isotopes. In the investigated nesosilicates and inosilicates, silicon isotope reduced partition function ratios (also called β-factors) show no correlation with the average Si-O bond length, which remains almost constant, but Si β-factors are correlated with the local chemical composition of the minerals. Fractional crystallization is one of the mechanisms, which could explain the evolution of iron isotopic compositions during magmatic differentiation. Using the present theoretical set of equilibrium fractionation factors allows us to assess the impact of inter-mineral isotopic fractionations, and shows that pyroxene appears to be the main mineral phase driving the isotopic evolution to a heavier signature in the most evolved lavas.

Keywords: DFT; Ab-initio; Isotopic fractionation; Silicates; Oxides; Stable isotopes; Iron; Silicon; igneous rocks; magmatic differentiation

1- Introduction

Silicon and iron represent, respectively, the second and fourth most abundant elements on Earth. Isotopic ratios of these elements are perfect candidates to become useful tracers of a variety of geological processes because of their ubiquitous nature. Despite the large mass difference between Fe isotopes (^{54}Fe, ^{56}Fe, ^{57}Fe, ^{58}Fe) and Si isotopes (^{28}Si,^{29}Si,^{30}Si), the magnitude of their high-temperature isotope fractionations is limited (e.g. Dauphas et al., 2012; Méheut et al., 2009; Savage et al., 2010; Teng et al., 2013; Williams et al., 2004; Zambardi et al., 2014). Iron is interesting because of its multiple oxidation states (Fe^0, Fe^{2+} and Fe^{3+}) that make it a perfect element to trace the redox conditions in igneous rocks such as the evolution of oxygen fugacity (fO_2) in the mantle associated with depth (Woodland and Koch, 2003; McCammon and Kopylova, 2004; Yaxley et al., 2012) or in the lavas during magmatic differentiation. In nature, silicon has two valence states (Si^0, Si^{4+}) (Poitrasson, 2017). Metallic silicon (Si^0) can be found in metallic inclusions in meteorites, and most likely in the metallic cores of terrestrial planets (e.g. Wai and Wasson, 1969; Georg et al., 2007; Pack et al., 2011). In the magmatic differentiation context, Si can be considered as only tetravalent. Silicon concentration increases during magmatic differentiation whereas Fe concentration decreases. Therefore, silicon isotopes are more likely reflecting cumulative effect (Zambardi et al., 2014). Considering their contrasted behavior during magmatic differentiation, Si and Fe isotopes represent complementary approaches to constrain the mechanisms of isotopic fractionation involved in magmatic differentiation. Both isotopic systems were extensively studied in that context, either independently (Weyer et al., 2005; Williams et al., 2005; Poitrasson and Freydier, 2005; Shahar et al., 2008; Teng et al., 2008; Schuessler et al., 2009; Schoenberg et al., 2009; Williams et al., 2009; Lundstrom, 2009; Savage et al., 2011; Sossi et al., 2012; Dauphas et al., 2014; Foden et al., 2014; Nebel et al., 2015; Poitrasson and Zambardi, 2015; Sossi and O'Neill, 2017; Williams et al., 2018; Li et al., 2020) or together (Zambardi et al., 2014; Gajos et al., 2016). Nonetheless, the processes leading to heavy Fe and Si isotopic compositions in the most evolved lavas during magmatic differentiation are still debated. Fractional crystallization (e.g. Schuessler et al., 2009; Sossi et al., 2012; Telus et al., 2012; Foden et al., 2015; Du et al., 2017), partial melting (Williams et al., 2009), fluid exsolution processes (Poitrasson and Freydier, 2005), thermal diffusion (e.g., Lundstrom, 2009; Zambardi et al., 2014; Gajos et al., 2016) and sulfide saturation in the magma (Williams et al., 2018) were suggested to explain the Fe systematics observed among igneous rocks. As Shahar et al. (2008) pointed out, "In order to understand the meaning of small but significant differences in Fe isotope ratios among minerals representing differentiated planetary materials, the mechanisms of high-T Fe isotope fractionation must be quantified".

Different techniques can be used to determine isotope fractionation factors in silicate minerals, including: 1) conventional analysis of mineral separates involving mineralization followed by iron or silicon separation by anion exchange chromatography and MC-ICP-MS analyses, for both natural or synthetic samples (Williams et al., 2005; Savage et al., 2011; Sossi and O'Neill, 2017; Shahar et al. 2008); 2) *In-situ* laser ablation coupled to MC-ICP-MS techniques using nanosecond or femtosecond laser on natural samples (Sio et al., 2013; Oeser et al., 2014; Oeser et al., 2015; Collinet et al., 2017; Oeser et al., 2018). 3) For Fe isotopes, the vibrational properties of minerals can be determined by nuclear resonance inelastic X-ray scattering (NRIXS) from which reduced partition function ratios, called β-factors, are derived (Dauphas et al., 2012; Dauphas et al., 2014; Roskosz et al., 2015); 4) Also for iron, β-factors can be calculated from second-order Doppler (SOD) shift derived from

Mössbauer spectroscopic measurements (Polyakov and Mineev, 2000; Polyakov et al., 2007; Polyakov, 2009; Polyakov and Soultanov, 2011); 5) Theoretical fractionation factors can also be determined from electronic structure calculations usually based on the density functional theory (Blanchard et al., 2009; Méheut et al., 2009; Huang et al., 2014; Méheut and Schauble, 2014; Wang et al., 2017). Concerning iron, only few fractionation factors are available for silicate minerals. Because olivine and most of pyroxenes are Fe^{2+}-bearing minerals, the Fe isotope fractionation between them is often considered as negligible (Dauphas et al., 2014; Roskosz et al., 2015) or even inexistent (Beard and Johnson, 2004). However, some studies on natural samples highlight small but distinct isotopic signatures for olivine and coexisting clinopyroxene and orthopyroxene (Zhu et al., 2002; Williams et al., 2005). This effect was also proposed earlier from Mössbauer data by Polyakov and Mineev (2000). Besides temperature, iron oxidation state is described as one of the main parameters influencing the iron isotope fractionation with the coordination number of iron (Polyakov and Mineev, 2000; Dauphas et al., 2014; Sossi and O'Neill, 2017). Indeed, Fe^{3+}-rich phases have stiffer bonds and therefore tend to concentrate heavy ^{57}Fe isotopes. This is the reason why most studies focused on the common Fe^{3+}-bearing oxide of magmas, i.e., magnetite, in order to constrain the isotopic evolution during magmatic differentiation (Polyakov and Mineev, 2000; Polyakov et al., 2007; Shahar et al., 2008; Dauphas et al., 2012; Sossi and O'Neill, 2017). Our study provides the first *ab-initio* values of inter-mineral fractionation factors for iron isotopes in silicate minerals. Regarding Si isotopes, only few theoretical studies were performed on high-temperature silicate minerals (Grant, 1954; Huang et al., 2014; Méheut and Schauble, 2014; Qin et al., 2016). Grant (1954) suggested that polymerization was the key factor influencing Si isotopes among the differentiation path with enrichment of heavy isotopes with increasing polymerization. The study of Poitrasson and Zambardi (2015) on lunar and terrestrial rocks supported Grant's hypothesis in displaying a clear relationship between increasing polymerization degree and increasing silicon isotope composition of lunar rocks. However, at the mineral scale, Méheut and Schauble (2014) displayed large isotopic fractionations between minerals having the same structure and silicon polymerization degree (kaolinite, lizardite). Silicon-Oxygen bond lengths (Huang et al., 2014) as well as the electronegativity of the cations Mg and Al (Méheut and Schauble, 2014) were also proposed to explain the difference in Si isotope signatures between minerals, but the effects of other cations have not been considered so far. Here, the influence of Ca, Fe, and Na on Si isotopes is tested through different silicate compositions.

The goal of the present study is to produce a consistent data set of iron and silicon β-factors representing the main Fe-bearing minerals of lavas. Four clinopyroxenes are investigated: aegirine, hedenbergite, augite and diopside as well as the most common orthopyroxene, i.e. enstatite. The olivine solid-solution is studied through four distinct compositions: fayalite, hortonolite and two forsterites (i.e. Fe-bearing and Fe-free forsterites). In addition, pure magnetite and ulvospinel were added to the study in order to model the fractionation factor between oxide and silicate minerals. This set of iron and silicon fractionation factors is obtained from first-principles quantum mechanical calculations. These data enable us to discuss the effect of different parameters (e.g. coordination number (CN), iron oxidation state, Fe-O and Si-O bond lengths, average or local chemical compositions) on the inter-mineral fractionation factors and to discuss the role of inter-silicate isotopic fractionation on the process of fractional crystallization that could explain the heavy Fe signatures of evolved lavas during magmatic differentiation.

2- Methodology

2.1- Calculation of equilibrium isotope fractionation factors

The equilibrium isotope fractionation factor *α(a,b,Y)* of an element Y between two phases a and b is defined as the ratio of isotope ratios and can also be written as the ratio of the reduced partition functions, called β-factors:

$$\alpha_{(a,b,Y)} = \frac{\beta_{(a,Y)}}{\beta_{(b,Y)}} \qquad \text{Eq. (1)}$$

Where $\beta(a,Y)$ can be seen as the equilibrium fractionation factor of *Y* isotopes between the phase *a* and a perfect gas of *Y* atoms. The reduced partition function ratio of each mineral was calculated from their harmonic vibrational frequencies (Bigeleisen and Mayer, 1947) using the following equation:

$$\beta(a,Y) = \left[\prod_{i=1}^{3N_{at}} \prod_{\{q\}} \frac{\nu_{q,i}}{\nu'_{q,i}} \frac{\exp(-\frac{h\nu_{q,i}}{2k_bT})}{1-\exp(-\frac{h\nu_{q,i}}{k_bT})} \frac{1-\exp(-\frac{h\nu'_{q,i}}{k_bT})}{\exp(-\frac{h\nu'_{q,i}}{2k_bT})}\right]^{1/(N\_q \times N)} \qquad \text{Eq. (2)}$$

where, $\nu_{q,I}$ and $\nu'_{q,I}$ are the vibrational frequencies of the heavy and light isotopologues in phase *a*, identified by a wavevector *q* and a branch index *i* from *1* to $3N_{at}$; N_{at} is the number of atoms in the crystal unit cell, *h* Planck's constant, k_b is Boltzmann's constant, and *T* the temperature (in Kelvin). The second product in Eq.(2) is performed on a sufficiently large grip of *Nq q*-vectors in the Brillouin zone. In Eq. (2), the three translational modes at the center of the Brillouin zone (Γ) with $\nu_{0,I} = 0$, are not considered. Equation (2) accounts for the fact that there should be no isotopic fractionation at the high-temperature limit, called the "rule of the high-temperature product" or "Redlich-Teller rule" (Bigeleisen and Mayer, 1947).

Isotope fractionation is often reported in permil (‰) and thus, we will adopt the usual notation: $10^3\ln\alpha(a,b,Y) = 10^3\ln\beta(a,Y) - 10^3\ln\beta(b,Y)$. In laboratory studies, $10^3\ln\alpha(a,b,Y)$ can be approximated (if alpha is not too different from 1) by the fractionation factor $\Delta_{a\text{-}b} = \delta_a - \delta_b$, where δ_a and δ_b represent the isotopic compositions of phases *a* and *b* in isotopic equilibrium, obtained as follows for iron isotopes:

$$\delta^{57}Fe\ (‰) = \left(\frac{\left({}^{57}Fe/{}_{54}Fe\right)_{sample}}{\left({}^{57}Fe/{}_{54}Fe\right)_{standard}} - 1\right) \times 1000 \qquad \text{Eq. (3)}$$

2.2- Modeling approach

The reduced partition function ratios of each mineral were calculated from Eq (2), using the phonon frequencies, $\nu_{q,I}$, computed from first-principles methods based on density functional theory (DFT).

Initial atomic positions and lattice parameters taken from experimentally determined structural models were relaxed first until the residual forces on atoms are less than 10^{-4} Ry/au, and the residual pressures smaller than 0.03 kbar. For each mineral, the dynamical matrix was calculated within density functional perturbation theory (DFPT) and then diagonalized for the two atomic masses of interest (54 and 57 for Fe / 28 and 30 for Si) in order to obtain the vibrational frequencies for both isotopologues. Structural relaxations as well as vibrational frequency calculations were performed using PWscf and PHonon codes included in the Quantum Espresso suite of codes (Giannozzi et al., 2009). All calculations were performed using the Perdew-Burke-Ernzerhof (PBE) parametrized generalized gradient approximation (GGA) functional (Perdew et al., 1996). The ionic cores were described by ultrasoft pseudopotentials (USPP) from the GBRV library (Garrity et al., 2014). The wave-functions cutoff was taken equal to 40 Ry for all minerals, such as the total energies are converged within 1 mRy/atom. A regular grid in k-space, shifted from Γ point, according to the Monkhorst-Pack scheme (Monkhorst and Pack, 1976) is used for Brillouin zone sampling. The size of the converged k-point grid for all the studied minerals is displayed in Table 1. For all minerals, vibrational frequencies were calculated along one shifted q-point except for magnetite vibrational frequencies that were calculated along a 2×2×2 shifted q-point grid. For the systems investigated here, the reduced partition function ratio converges rapidly with respect to the number of q-points. Shifting the q-point grid relative to the center of the Brillouin zone (Γ point) avoids us to deal with the long-range effects that should be considered otherwise. Such long-range effects give rise to the LO-TO frequency splitting and thus affect the reduced partition function ratios.

As mentioned above, experimental structures were taken as starting configurations. However, in the investigated silicate minerals, there are two sites available for iron (M_1, M_2) that are shared by other cations such as Mg, Ca or Na and experimental models could only give us the occupation proportion of iron in each site. Thus, we performed self-consistent field (scf) calculations on each structure for all non-equivalent iron atomic positions in M_1 and M_2 sites, with various magnetic moments, in order to find the configuration with the lowest energy to perform the calculation of the phonon frequencies (Fig. A1 in Appendix). Calculations for all minerals were spin-polarized and magnetic moments were free to relax. Iron electronic charge density of the optimized structures were determined using the Bader Charge Analysis code (Henkelman et al., 2006). Bader (2001) developed a method based on zero flux surfaces to divide crystal/molecule in atoms. By doing so, the charge enclosed in the Bader volume approximates the total electronic charge of the atom.

3- Results

3.1- Structural properties

In terms of structure, olivine is a nesosilicate that consists of isolated silicon tetrahedra connected by interstitial cations, with the general formula $[M_2][M_1](T)O_4$ where T is the tetrahedral site preferentially occupied by Si and occasionally Al or Ti and M_1 and M_2 are octahedral sites occupied mainly by Fe^{2+}, Mg, Mn, Ni. Pyroxenes are part of the inosilicate group with the general formula $[M_2][M_1](T)_2O_6$ where the six-coordinated M_1 site is occupied mainly by Mg, Fe^{2+}, Fe^{3+}, Al, Ti, and the five to eight coordinated M_2 sites by Mg, Fe^{2+}, Na, Ca. The tetrahedral sites are occupied by Si and

minor Al, Ti or even Fe^{3+}. Substitution of Mg^{2+} by Fe^{2+} in pyroxene can create distortion of M_1 octahedra (Cameron and Papike, 1981), as iron ions are larger.
The general formula of the spinel group is AB_2O_4. In magnetite, A cations represents Fe^{2+} in the octahedral M sites and B represents Fe^{3+} in tetrahedral T site and octahedral M sites. A substantial amount of titanium can enter in the magnetite structure, forming a continuous solid solution between magnetite and ulvospinel. In ulvospinel, A represents tetravalent (Ti^{4+}) and B the divalent (Fe^{2+}) cations. In this study, A cations occupy the octahedral M sites and B cations occupy both octahedral M and tetrahedral T sites (Barth and Posnjak, 1932).

As described above, pyroxenes are not restricted to a single chemical composition in nature: proportion of the different cations such as iron, magnesium, sodium and calcium bound to the Si-O structure can evolve from 0 to 100%. In order to reproduce common Fe-bearing clinopyroxene compositions of various magmatic rocks, we modeled the end-members aegirine ($FeNaSi_2O_6$) and hedenbergite ($FeCaSi_2O_6$) as well as intermediate compositions such as augite ($Mg_{0.25}Fe_{1.25}Ca_{0.5}Si_2O_6$) and diopside ($Mg_{0.75}Fe_{0.25}$)$CaSi_2O_6$. For the most common orthopyroxene, enstatite, we chose the same composition (($Fe_{0.125}Mg_{0.875}$)$_2Si_2O_6$) as the sample analyzed by NRIXS spectroscopy in Dauphas et al. (2012). Four compositions of the olivine solid-solution were studied: the two end-members, fayalite (Fe_2SiO_4) and forsterite (Mg_2SiO_4), as well as two intermediate compositions, hortonolite ($FeMgSiO_4$) and Fe-bearing forsterite ($Fe_{0.125}Mg_{0.875}SiO_4$) in order to better assess the impact of iron concentration on the olivine solid solution. Concerning the oxides, pure ulvospinel (Fe_2TiO_4) as well as magnetite (Fe_3O_4) were studied.

The clinopyroxene and olivine unit cells contain four formula units, and the orthoenstatite and ulvospinel unit cells contain eight formula units (Table 1). Primitive cells were sufficient to proceed to multiple Fe-Mg substitutions among the different silicate compositions and to have a realistic representation of mineral structures. Space groups for each mineral are displayed in Table 1. All non-equivalent iron positions as well as the spin state and magnetic ordering, were tested by doing self-consistent field calculations in order to find the model having the lowest energy (Fig A1 and Table A1 in Appendix), on which phonon calculations were performed. Concerning Fe-bearing forsterite, two iron non-equivalent positions were tested and the model where iron is in M_1 site displays the lowest energy by about 7.02 kJ/mol. This energy difference can be interpreted as iron being preferentially in M_1 sites compared to M_2 sites. Following the same approach as Umemoto et al. (2011), we assessed the percentage of iron in each site. Our results suggest that 72% of iron will preferentially be incorporated in M_1 sites over M_2 sites at 700°C. This calculation is consistent with our modeled hortonolite that has 75% of the iron in M_1 sites. It also agrees with the study of Brown and Prewitt (1973), indicating that iron is mainly in M_1 sites in hortonolite. However, we decided to perform phonon calculation on both forsterite models in order to assess the impact of iron positions on the $^{57}Fe/^{54}Fe$ β-factors as this element can be equally distributed in M_1 and M_2 sites at high temperature in forsterite of the upper mantle (e.g. Blanchard et al., 2017; McCarty et al., 2015). Regarding ulvospinel, the positions of iron in the octahedral and tetrahedral sites are based on Gatta et al. (2014) in order to result in an asymmetric charge distribution which, preserve the non-cancelling cation-cation repulsions and the observed out-of-center distortion of the central Ti^{4+} (Kunz and David Brown, 1995). As ulvospinel is antiferromagnetic (Gatta et al., 2014), only one spin configuration was compatible with an antiferromagnetic structure that consists of all the Fe_T in spin up configuration and all the Fe_M in spin down configuration. Magnetite is known to be ferrimagnetic, and the spin

configurations were taken from Wright et al. (2002), where the Fe_T is in spin down configuration and all the Fe_M in spin up configuration.

For the end-members of the solid solutions (i.e., aegirine, hedenbergite, fayalite) and for diopside where all iron positions are equivalent, only the magnetic order was investigated. Fayalite is known to be antiferromagnetic. The spin configuration is taken from Cococcioni et al. (2003) where the magnetic ground state corresponds to a similar Fe_{M2} magnetization to that of the closest Fe_{M1} site and the antiferromagnetic ordering occurs between corner-sharing octahedra (Fig. A1 in Appendix). As there is no information about the spin configuration of the antiferromagnetic hortonolite, we decided to take the same spin configuration as for fayalite (Fig. A1 in Appendix). Concerning Fe-bearing forsterite, the unique iron atom (in M_1 or M_2 site) is high spin. In hedenbergite and aegirine, iron is only located in M_1 site, half of the Fe_{M1} are set up with spin up polarization and the other half with a spin down polarization. In augite, where iron atoms are distributed between M_1 and M_2 sites, the spin polarization has been set up in order to get an antiferromagnetic ordering occurs between corner-sharing octahedra (Fig. A1 in Appendix). As structure with 2 Fe_{M1} and 1 Fe_{M2} with spin up polarization and the others as spin down polarization (Fig. A1 in Appendix, conf. C). In enstatite (config. F in Fig A1) and diopside, iron is arranged in high-spin state.

Calculated lattice parameters for the most stable model of each mineral agree with the experimental values within 1-2% (Table 1). The Fe-Fe interchain distance in hedenbergite (6.534 Å) is larger than in aegirine (6.352 Å) as described in Baum et al. (1997) that displays an Fe-Fe interchain distance 4.7% larger in hedenbergite than in aegirine. The distortion of Fe^{2+} octahedral sites in augite and enstatite is observed in the modeled structures in accordance with experiments (Cameron et al., 1973; Cameron and Papike, 1981).

3.2- Reduced partition function ratios of iron and silicon

Temperature dependence of the Si and Fe reduced partition function ratios of the silicate and oxide minerals are displayed in Fig 1. The parameters of the corresponding polynomial fits are given in Table 2. A linear correlation between β-factors and their corresponding average force constants (F) is observed for iron and silicon (Fig. 2), where F corresponds to the average of the force constants for an atom X in three orthogonal directions. This parameter F is calculated for each crystallographic site where atom X is located and averaged in order to obtain an average force constant for each mineral. This linear relationship allows us to discuss isotopic fractionations in terms of both β-factors or force constants. Following the general discussion on the uncertainties related to the harmonic approximations and the PBE functionals performed by Méheut et al 2009, a systematic relative uncertainty of about 5% can be applied to each β-factor, and force constant calculated in this study.
At 1000 K, the whole set of $10^3 ln\beta^{57}Fe/^{54}Fe$ spans in a range of 0.5 ‰ and the $10^3 ln\beta^{30}Si/^{28}Si$ are within a range of 1 ‰. All studied minerals are enriched in ^{57}Fe and in ^{30}Si with respect to fayalite. The highest iron β-factors are found in the Fe^{3+}-bearing minerals, aegirine and magnetite. The highest silicon β-factors are found in forsterite and enstatite. It is noteworthy that forsterite displays different $10^3 ln\beta^{57}Fe/^{54}Fe$ when the sole iron of the unit cell is in M_1 or M_2 site. Indeed, the forsterite-M1 configuration, that is the most energetically favorable (part 3.1), displays a higher $10^3 ln\beta^{57}Fe/^{54}Fe$ of about 0.094 ‰ at 980 K compared to the Forsterite-M2 configuration.

4- DISCUSSION

4.1 – Parameters controlling Fe isotope fractionation in minerals

As mentioned, the reduced partition function ratios calculated from equation (2) correlate linearly with the corresponding average force contants, $\langle F \rangle$ (Fig. 2). This observation is in agreement with the following relationship (Bigeleisen and Mayer 1947):

$$1000 \ln \beta = 1000 \left(\frac{1}{m'} - \frac{1}{m}\right) \frac{\hbar^2}{8 k_b^2} \frac{\langle F \rangle}{T^2} \qquad \text{Eq. (4)}$$

Where *m'* and *m* are atomic masses of the light and heavy isotopes respectively. Compared to the frequency-based equation (2), the force constant-based equation (4) implies some approximations (i.e. $h\nu/k_B T \leq \sim 2$ and harmonic approximation). The divergence between the two equations increases when masses and temperature decrease (Blanchard et al., 2017). In the case of iron, the constant of proportionality of the approximate equation (4) (i.e. $1000 \ln \beta\, {}^{57}Fe/{}^{54}Fe = 4284 \langle F \rangle / T^2$) is indeed very close to the one derived from Figure 2 and therefore from equation (2) at the high temperature of 1280 K (i.e. $1000 \ln \beta\, {}^{57}Fe/{}^{54}Fe = 4274 \langle F \rangle / T^2$), but deviates as expected from the relationship that we can calculate at room temperature (i.e. $1000 \ln \beta\, {}^{57}Fe/{}^{54}Fe = 4054 \langle F \rangle / T^2$, for T = 298K).

4.1.1 – Fe-O bond length

Sossi and O'Neill (2017) displayed a negative relationship between force constant and the Fe-O bond length, with the stiffest bonds (shortest bonds associated with the largest force constant) corresponding to minerals enriched in heavy isotopes ^{57}Fe. Here, the relationship between iron force constant and the average Fe-O length is more blurred (Fig. 3a). Magnetite and ulvospinel are the only mineral considered here having iron in tetrahedral site. These minerals also have iron in octahedral site. As expected, tetrahedral iron, with shorter bonds, displays a larger interatomic force constant than octahedral iron. Within the Fe-bearing silicates, one can see a general trend where octahedral sites associated with shorter average Fe-O bond lengths show larger force constants. However, if we consider for example the pairs M_1-Augite/M_1-Forsterite or M_1-Fayalite/M_1-Hortonolite. Both mineral sites of each pair have the same average Fe-O bond length but very different iron force. Iron in the M_1 site of forsterite has a force constant 13% larger than in augite, and iron in the M_1 site of hortonolite has a force constant 29 % larger than in fayalite. Therefore, the iron isotope fractionation between these minerals cannot be explained solely by a difference of Fe-O bond lengths.

One can also choose to look at the correlation between the iron force constant and the iron polyhedral volume (fig. 4a). Depending on the type of distortion of the octahedra, the polyhedral volume might be a better parameter than the average bond length. Figure 4a shows that the mineral pairs mentioned above (M_1-Augite / M_1-Forsterite or M_1-Fayalite /M_1-Hortonolite) move in direction of a better correlation, with larger force constants associated with smaller volumes. However, the general trend is not improved significantly, supporting the importance of other parameters.

4.1.2 – Iron electronic charge density

One of the main characteristics of iron is its redox sensitivity. As described by Polyakov and Mineev (2000) and subsequent studies (Blanchard et al., 2009; Dauphas et al., 2012; Polyakov et al., 2007; Roskosz et al., 2015; Shahar et al., 2008; Sossi and O'Neill, 2017), Fe^{3+}-bearing minerals, such as magnetite, display a heavier isotopic signature compared to Fe^{2+}-bearing minerals. As mentioned in the method section, the valence of iron is approximated by the Bader charge (Bader, 2001). Except for aegirine that is a Fe^{3+}-bearing mineral and magnetite that contains both Fe^{3+} and Fe^{2+}, all minerals are only bearing Fe^{2+}. Here, we observe that all minerals display a mean valence number of about 1.4 (Fig. 4b). Aegirine shows a valence of 1.8 and magnetite shows an intermediate valence of 1.5. Here again, the results suggest that the iron oxidation state strongly affects the iron force constant and therefore the isotopic fractionation. Aegirine as well as magnetite, the trivalent Fe-bearing minerals, display significantly higher force constants than all other minerals that contain only divalent iron. However, within Fe^{2+}-bearing minerals, there is no clear correlation between the Bader charge and the force constant. For nearly the same value of the Bader charge, the iron force constant varies over more than 50 N/m.

4.1.3 – Iron concentration

Dependency of the reduced partition function ratio of an element on its concentration in a mineral has been underlined for several stable isotope systems. For example, Wang et al. (2017) showed that the Ca concentration in pyroxenes affects the equilibrium Ca isotope fractionation down to very low concentrations (x = 1/48, corresponding to the molar ratios of $Ca_xFe_yMg_{1-x-y}SiO_3$). These authors also highlighted that Fe concentration, to a lesser extent, has an impact on Ca isotope fractionation with addition of Fe in orthopyroxene leading to a lower $\ln\beta$ $^{44}Ca/^{40}Ca$. In the present study, we can also see an effect of iron concentration in the minerals on their iron β-factors for a given mineral solid-solution (Fig 4c). In the olivine solid-solution, the iron β-factor decreases with increasing iron content. Fayalite has the lowest iron force constant, forsterite the highest while hortonolite shows an intermediate value. The same trend is observed for the three Fe^{2+}-bearing clinopyroxenes, namely augite, hedenbergite and diopside. Note that because of the presence of trivalent iron, aegirine is outside this clinopyroxene trend. We also observe that the orthopyroxene enstatite has a slightly higher force constant than the clinopyroxene diopside while the iron content is the same.

4.1.4- Iron second neighbors

Coordination number as well as iron oxidation state can explain major fractionation effects between Fe-bearing minerals. However, the scattered correlations displayed in previous sections can be explained by the iron local environment in the silicates. Indeed, for Fe^{2+}-bearing minerals displaying the same coordination number, the only parameters that lead to different fractionation are the nature and the number of the surrounding cations (i.e. Fe, Mg, Ca and Na). The best illustration of this is the olivine solid solution where iron is only present as Fe^{2+} and with nearly the same Fe-O bond lengths (Fig 3a). In olivine, iron in the M_1 octahedral site is surrounded by 4 cationic neighbors sharing an edge and 8 cationic neighbors sharing a corner while iron in the M_2 site has 2 cations sharing an edge and 10 sharing a corner. Edge-sharing neighbors are within 3.2 Å from the central

iron while corner-sharing cations are located beyond 3.6 Å. The Fe/Mg ratio in these neighboring sites will affect the force constant of the central iron, whether located in M_1 or M_2 sites. The more iron is present among these cationic neighbors, the weaker is the iron force constant (fig. 5a). This is especially noticeable when looking at the force constant evolution in M_1 sites. The decrease is less apparent for M_2 sites, and this could be explained by the fact that there are only 2 neighbors sharing an edge in M_2 sites against 4 in the M_1 sites. This would mean that the closest cations from the central iron affect more the iron force constant. So, the force constant is not only related to the nature of the second neighbors (or first cationic neighbors) but also to their number and crystallographic arrangement.

The effect of the local cationic environment leads to an average correlation between reduced partition function ratios and iron concentration in the minerals (Fig. 5, large symbols). However, the effect of the local environment cannot only be reduced solely in term of concentration of iron in the minerals. As described above in part 4.1.4, Wang et al. (2017) showed that Ca concentration in pyroxenes has no effect on Ca fractionation factor for small Ca concentration below x = 1/48. From our observations, this concentration limit could correspond to the point where the local environment of Ca does not change anymore. Our conclusion also agrees with Roskosz et al. (2015) that underlined that the iron force constant of Cr-bearing spinel is much lower (244 ± 22 N/m) than the Cr-free spinel (296 ± 18 N/m) and explained it as the effect of Cr substitution by Al in the octahedral sites. Moreover, the impact of second neighbors have been observed by Ducher et al. (2016) on zinc isotopes in the case of zincite and franklinite that display different $\ln\beta^{66}Zn/^{64}Zn$ despite the fact that both minerals have the same Zn-O bond lengths and coordination number (4-fold). The only difference is the nature of the second neighbors, iron for franklinite and zinc for zincite. This observation could also explain the difference of iron force constant between dacite and rhyolite glasses with similar Fe^{3+}/Fe_{tot} in Dauphas et al. (2014): substitution of Ca for K in dacite or for Na in rhyolite as second neighbor of iron atoms could at least partly explain this variation in β-factors.

4.2 – Parameters controlling Si isotope fractionation in minerals

In contrast to iron, silicon is not a redox sensitive element in silicic melts and the concentration of silicon is constant in the different silicate groups studied. As a result, the evolution of the silicon force constant in the olivine solid-solution or in the pyroxene group cannot be addressed by a change in silicon concentration. In order to examine the variations in Si β-factors (Fig. 1b), we focus here on bond lengths and the nature of the second neighbors.

4.2.1 - Si-O bond length

The relationship between silicon force constant and the average Si-O bond length is inexistent in the olivines and pyroxenes investigated here (Fig 3b). In silicon tetrahedra, the Si-O bond lengths show negligible fluctuations around 1.67 Å, while the Si force constant ranges between 608 and 700 N/m. This implies that a parameter other than the Si-O bond length controls the Si isotope fractionation in both olivine and pyroxene groups. This is supported by the theoretical study of Huang et al. (2014) that found similar average Si-O bond length for olivine, clinopyroxene and orthopyroxene of about 1.64 Å. This is also supported by Méheut and Schauble (2014) and Qin et al. (2016) who observed a well-defined correlation between Si-O bond length and Si β-factor for most silicates except for forsterite, enstatite, and clinopyroxenes. Qin et al. (2016) noted, however, that these minerals fall on

the correlation if the Si-O polyhedron volume is considered instead of just the mean Si-O bond length (their Fig. 5). This is not the case in the present study. In addition, the various clinopyroxenes display the same silicon polymerization but distinct force constants, upholding that polymerization of SiO_4^{4-} is not the key factor causing silicon isotope fractionation in silicate minerals (Méheut and Schauble, 2014; Qin et al., 2016). Huang et al. (2014) highlighted the fact that Si isotopes can fractionate between minerals with similar coordination number if their Si-O bond lengths are different. Here, we go one step further in showing that Si isotopes can fractionate between minerals where silicon has the same coordination number and very similar average bond lengths.

4.2.2- Silicon second neighbors

As described for Fe isotopes, it seems that the nature of the silicon second neighbors is the major parameter affecting its force constant among olivines and pyroxenes. In the olivine solid-solution, silicon is, by definition, in an isolated oxygen tetrahedron sharing 3 edges and 6 corners with iron or magnesium octahedra. Here, we identified, as we did for iron, the nature of each cation sharing an edge or corner with the central silicon. Results are displayed in Fig 5b. It is clear that the Si tetrahedron sharing edges and corners with only iron atoms in fayalite displays a lower Si force constant (608 N/m) compared to the one sharing edges and corners with only magnesium atoms in forsterite (700 N/m), with intermediate compositions in between. Aegirine and hedenbergite are also good examples as they have the same structure (Appendix– Fig A2) and differ only by the substitution of Na (aegirine) to Ca (hedenbergite) in M_1 sites. In these clinopyroxenes, a Si atom is surrounded by 9 atoms: 2 Na/Ca atoms sharing an edge with the Si tetrahedron and 7 atoms (2 Si, 2 Ca/Na and 3 Fe) sharing the corners. As a result, the substitution of the Ca by Na in aegirine in the local environment of Si modifies the average force constant from 654.9 N/m to 647.8 N/m. The nature and number of second neighbors has thus definitely an impact on Si force constant and therefore on Si β-factor (fig 5b).

Méheut and Schauble (2014) discussed that electronegativity of the cations may have an impact on Si isotopes. Depending on the electronegativity difference between Si and neighboring cations, the distribution of the electronic density is modified, the bridging oxygen receive more or less electrons affecting in turn the Si-O bond strength. In their phyllosilicate study, Méheut and Schauble (2014) found that the presence of cations with lower electronegativity (Ca, Na compared to Mg) leads to lighter silicon isotopic signature. This conclusion is true for the geometrical arrangement of cations in the phyllosilicate structure, but as these authors already suggested, this conclusion does not hold for olivine. In phyllosilicates, the presence of cations with lower electronegativity brings more electrons on the bridging oxygen. The Si-O apical bond becomes stronger but the equatorial bonds counteract this effect by weakening, leading to an overall lowering of the Si force constant (see Fig. 9 of Méheut and Schauble, 2014). In olivine, because of the more isotropic distribution of the cations around Si atom, there is no such counterbalancing effect. Replacing Mg atoms (χ_{Mg} = 1.31 under Pauling's definition) by more electronegative Fe atoms (χ_{Fe} = 1.83) decreases the electronic charge of oxygen atoms (i.e. Bader charge of oxygen atoms decreases from 1.83 in forsterite down to 1.66 in fayalite) and therefore decreases the Si force constant. In olivine solid-solution, this electronegativity effect is also enhanced by structural relaxations that lead to Si-Fe distances in fayalite 1.5% longer than Si-Mg distances in forsterite. These longer distances in fayalite contribute to the decrease of Si force constant. Our results on olivine agree with the measurements done by Savage et al. (2011) on

natural samples. The Si isotope fractionations between plagioclase and olivine of various compositions indeed suggest that olivine Si β-factor decreases with increasing iron content.

4.3 – Comparison with previous data

4.3.1 – Fe isotopes

We compare our ab-initio iron isotope fractionation β-factors and iron force constants (part 3.2) with previous values reported in the literature. The available experimental and theoretical β-factors are displayed in Fig. 6. One must note that the uncertainties of NRIXS and Mössbauer results for the various minerals are respectively in the order of ≤ 0.05 ‰ and 0.10 ‰. And applying the general 5% of relative uncertainty on DFT results would lead to an error bar of maximum ± 0.03 ‰.

The general trend of the silicate β-factors is similar, whatever the techniques used, displaying that, at equilibrium, aegirine is with magnetite the most enriched in ^{57}Fe followed by ulvospinel, enstatite and forsterite. Slightly below are diopside, hortonolite, augite, hedenbergite and fayalite. Considering the uncertainties, our theoretical β-factors are lower than the β-factors determined by NRIXS measurement for forsterite (Dauphas et al., 2014) and the approximate theoretical calculations for fayalite from Sossi and O'Neill, (2017). In contrast, our β-factors are higher for enstatite and lower for aegirine and magnetite, than those determined from Mössbauer measurements (Polyakov and Mineev, 2000). All other values agree within uncertainties (Fig. 6a). The discrepancies between theoretical and Mössbauer β-factor values might be due to the slight chemistry difference between the minerals or/and to the quality of the Mössbauer data used. Indeed, the first value for magnetite β-factor in Polyakov and Mineev (2000) using Mössbauer SOD shift from De Grave et al. (1993), appeared to be overestimated compared to subsequent magnetite β-factors measurements (Mineev et al., 2007; Polyakov et al., 2007; Dauphas et al., 2012; Sossi and O'Neill, 2017). Discrepancies between Mössbauer-derived and DFT-based β-factors have also been observed for pyrite (Polyakov and Mineev, 2000; Blanchard et al., 2009; Blanchard et al., 2012). Polyakov et al. (2019) showed that the Mössbauer temperature (θ) used in Polyakov and Mineev, 2000 were erroneous by recording a new Mössbauer spectra of pyrite. Pyrite β-factor calculated from this revised Mössbauer data is in good agreement with that obtained by DFT calculations (Blanchard et al., 2009) and by NRIXS measurements (Polyakov et al., 2013). With this in mind, one cannot exclude that aegirine and enstatite β-factor calculated in Polyakov and Mineev (2000) using De Grave and Van Alboom (1991) data could be erroneous for the same reason.

A general advice is to avoid combining β-factors obtained from different techniques, whenever possible. Due to systematic errors, relative values (i.e. isotopic fractionation between two phases) within a same technique are expected to be more accurate than differences taken from two distinct techniques. Looking at the olivine solid-solution, one could have doubts about the reliability of the 68 N/m difference between the forsterite iron force constant calculated from NRIXS measurement by Dauphas et al. (2014) and the fayalite one approximated from theoretical calculation using Born-Landé equation (Young et al., 2009) by Sossi and O'Neill (2017). However, our DFT approach, where the two end-members have been treated in a consistent way, provides a significant difference too (47 N/m) and thus supports the existence of a Fe isotope fractionation at equilibrium between forsterite and fayalite.

The calculated iron force constant of magnetite (F = 207 N/m) is in agreement with the NRIXS-derived iron force constant of Polyakov et al. (2007) of 228 ± 15 N/m later revised downwards by Mineev et al. (2007) to 198 ± 15 N/m. The calculated $\Delta^{57}Fe_{Mag\text{-}Fay}$ = +0.44 x $10^6/T^2$ overlaps with the $\Delta^{57}Fe_{Mag\text{-}Fay}$ = +0.40 x $10^6/T^2$ determined by Sossi and O'Neill (2017). The $\Delta^{57}Fe_{Mag\text{-}Fay}$ = = +0.30 x $10^6/T^2$ calibrated experimentally using the three-isotope method by Shahar et al. (2008) is lower than our calculated $\Delta^{57}Fe_{Mag\text{-}Fay.}$ However, looking at the only fully equilibrated experiments 'QFM 8' of Shahar et al. (2008) the estimated $\Delta^{57}Fe_{Mag\text{-}Fay}$ is about +0.40 x $10^6/T^2$ (Sossi and O'Neill, 2017). Ulvospinel is poorly studied for iron isotopes, however some spinels were studied such as Al-rich spinels (Polyakov and Mineev, 2000) and Ti-free spinels (Roskosz et al., 2015). Ulvospinel in our study displays an average iron force constant of about 151.8 N/m when Polyakov and Mineev (2000) reported a force constant of 106 N/m for their Fe^{2+}-spinel ($Mg_{0.9}Fe_{0.1}Al_2O_4$), and Roskosz et al. (2015) found a much higher value for their Fe^{2+}-spinel of about 196 N/m. Beyond the limitations related to the use of different techniques as discussed above, the difference in term of cationic compositions of the three types of spinel studied may be the reason of such apparent iron force constant differences between these Fe^{2+}-minerals.

Iron isotope fractionation factor between olivines and pyroxenes were also determined on natural samples, especially from mantle xenoliths, in various studies (e.g.. Beard and Johnson, 2004; Williams et al., 2004; Weyer and Ionov, 2007; Schoenberg et al., 2009). At relevant mantle temperature (1100K), our calculated $\Delta^{57}Fe/^{54}Fe_{diopside\text{-}forsterite}$ = -0.03 is identical, within 2 standard deviation uncertainties, to the mean $\Delta^{57}Fe/^{54}Fe_{cpx\text{-}ol}$ of about 0.04 ± 0.08‰ measured by Weyer and Ionov (2007) in lherzolite. Schoenberg et al. (2009) measured a $\Delta^{57}Fe/^{54}Fe_{augite\text{-}ol}$ = 0.10 ± 0.05 ‰ that is close to the calculated $^{57}Fe/^{54}Fe_{augite\text{-}fayalite}$ = 0.14 ‰ at 923 K. Moreover, the $\Delta^{57}Fe/^{54}Fe_{cpx\text{-}ol}$ from Williams et al. (2004) of about 0.09 ‰ ± 0.07 obtained on natural samples by mineral separation and solution analysis falls in the range of the calculated $\Delta^{57}Fe/^{54}$ $Fe_{diospide\text{-}fayalite}$ = 0.15‰ and $\Delta^{57}Fe/^{54}$ $Fe_{diospide\text{-}hortonolite}$ = 0.01 ‰ at T ≈ 1273 K (minerals reflecting the most likely composition of natural samples). Beard and Johnson (2004) determined $\Delta^{57}Fe/^{54}Fe_{cpx\text{-}ol}$ between -0.06 ± 0.14 ‰ and 0.28 ± 0.14 ‰ and $\Delta^{57}Fe/^{54}Fe_{opx\text{-}ol}$ between -0.18 ± 0.14 ‰ and 0.28 ± 0.14 ‰ at magmatic temperature (between 1108 and 1373K) while Zhu et al. (2002) measured a mean $\Delta^{57}Fe/^{54}Fe_{cpx\text{-}ol}$ = 0.28 ± 0.12 ‰ and a $\Delta^{57}Fe/^{54}Fe_{opx\text{-}ol}$ = 0.32 ± 0.12‰. Our calculated values ($\Delta^{57}Fe/^{54}Fe_{diopside\text{-}forsterite}$ ≈ -0.03 ‰ and $\Delta^{57}Fe/^{54}Fe_{enstatite\text{-}forsterite}$ = 0.01 ‰ at the same temperature range) fall within the wide fractionation range measured by Beard and Johnson (2004). These observations as well as the relationship between the $\partial^{57}Fe$ and Fe concentration of clinopyroxenes pointed out in Beard and Johnson (2004), may suggest that a number of the measured iron isotope fractionation factors in the various studies reflect the equilibrium fractionation. However, some iron fractionation factors measured by Beard and Johnson (2004), Schoenberg et al. (2009) and Zhu et al. (2002), are slightly higher than the ones calculated in this study. This slight difference between the measured and calculated iron isotope fractionation factors could be explained by the compositional difference of the mineral phases but could also reflect an isotopic disequilibrium, as concluded by Beard and Johnson (2004) on the basis of mineral delta-delta plots. Previous studies displayed indeed the importance of kinetic effects on iron isotope fractionation in natural samples (e.g. Teng et al., 2011; Sio et al., 2013; Oeser et al., 2015; Collinet et al., 2017; Dauphas, 2017; Oeser et al., 2018).

In summary, the fractionation factors calculated here is a stand-alone set that can be used for a majority of magmatic series, due to its large variety of mineral compositions. This will avoid introducing additional uncertainties related to the use of β-factors derived from different methods.

4.3.2 – Si isotopes

Silicon isotope fractionation between silicates and metals in the context of core formation has been extensively studied in the past years (Georg et al., 2007; Ziegler et al., 2010; Shahar et al., 2011; Armytage et al., 2012; Javoy et al., 2012; Zambardi et al., 2013; Pringle et al., 2014; Poitrasson, 2017). However, only few studies concern silicon isotope fractionation between silicates themselves in the context of magmatic differentiation (Méheut et al., 2009; Huang et al., 2014; Méheut and Schauble, 2014; Qin et al., 2016). Among these studies, Huang et al (2014) and Qin et al. (2016) calculated from first-principles methods a large variety of silicate mineral β-factors such as for olivine, clinopyroxene and orthopyroxene with a limited cationic environment (Ca, Mg). Our results agree with their previous calculations showing the evolution olivine > orthopyroxene > clinopyroxene in terms of ^{30}Si enrichment (Fig. 6b). However, the absolute values of the β-factors exhibit systematic differences (Fig. 6b) which can be explained in different ways. Firstly, the calculations of Huang et al. (2014) were performed at zero-pressure and T = 300K, whereas Qin et al. (2016) performed calculations at zero-pressure and T = 0K, using both the same LDA functional. Since the volume expands with increasing temperature, the β-factors calculated by Huang et al. (2014) shifts to lower values with respect to those by Qin et al. (2016). Secondly, our calculations were performed at zero-pressure and zero-temperature like in Qin et al. (2016), but using the GGA-PBE functional instead of the LDA one. We thus found equilibrium volumes about 7% larger than in the study of Qin et al. (2016) for the three minerals. This observation, that explains our lower β-factors, is consistent with the general knowledge of the functional effect on the bond lengths description. LDA functional is known to underestimate by 2-3 % the experimental volumes (e.g. Qin et al. 2016) whereas GGA functionals tend to overestimate them (Table 1). Thus, the computational parameters likely explain this systematic difference on β-factors, but do not affect the inter-mineral fractionations. This emphasizes again the importance of using a consistent data set to compute inter-mineral isotopic fractionations. Lastly, in addition to these temperature and functional effects, one must note that the pyroxenes in the present study have some atoms of iron in their M sites whereas the pyroxenes in the previous studies were iron-free. Following our observations, the nature of second atomic neighbors likely impacts the Si β-factors. For instance, in the olivine solid-solution, having iron atoms as silicon second neighbors lowers the Si force constant, and as a consequence the Si β-factor.

4.4 – Geochemical implications on magmatic differentiation

In many studies, the Fe isotope fractionation factor between the melt and olivine ($\Delta_{melt\text{-}olivine}$) is considered to represent $\Delta_{melt\text{-}Fe^{2+}\ silicates}$ (e.g. Dauphas et al., 2014; Sossi et al., 2012). In a core-mantle differentiation context or in less differentiated planetary bodies than Earth, pyroxenes have mainly the composition of enstatite and olivines are forsterite-like. In these contexts, calculations agree that there is no significant Fe isotope fractionation between silicate minerals. This inference is supported by experimental determination of isotopic partitioning (Prissel et al., 2018) and interplanetary comparisons (Poitrasson et al., 2019). However, considering the upper crust formation, our results

evidence significant iron isotope fractionation between Fe^{2+}-bearing minerals, even with similar Fe-O bond lengths. The use of our set of isotopic fractionation factors for modeling the fractional crystallization occurring during magmatic differentiation can help to assess the role of Fe^{2+}-bearing silicates on the iron heavy signature of the granites and evolved volcanic lavas compared to basalt. Here, simple models are performed based on Rayleigh equation:

$$R = R^0 \, f^{\alpha_{bulk}-1} \qquad \text{Eq. (5)}$$

Where, R is the $^{57}Fe/^{54}Fe$ isotopic ratio and R^0 is the initial ratio, ƒ is the fraction of remaining melt and α_{bulk} represent the bulk fractionation factor between residual melt and crystallizing minerals computed according to Eq. 6 as described below.

We used the Magma Chamber Simulator (MCS; Bohrson et al., 2014) based on MELTS software (Gualda et al., 2012) in order to model fractional crystallization of an andesitic melt as in Dauphas et al. (2014) that simulates the formation of peraluminous A-type granite with QFM (Quartz-Fayalite-Magnetite) buffer (See calculation details in the Supplementary Tables). In the MCS, composition and proportion of the minerals removed from the melt are described every 5°C step, during a temperature drop from 1165°C to 885°C. From this information, the bulk fractionation factor is calculated by taking the calculated mineral-melt fractionation factor (α_1, …, α_n) weighted by their proportions (X_1 , …, X_n) :

$$\alpha_{bulk} = \alpha_1 \times X_1 + \cdots + \alpha_n \times X_n \qquad \text{Eq. (6)}$$

Mineral β-factors are taken from the present study. In order to reproduce the evolution of the melt β-factor during magmatic differentiation, the iron β-factor of the melt was calculated from the sigmoidal equation of the iron force constant proposed by Dauphas et al. (2014) from NRIXS measurements of synthetic glasses:

$$F = F^0 + 41\left(1 + e^{34-\frac{SiO_2}{2}}\right) \qquad \text{Eq. (7)}$$

The iron force constant value of the initial melt F^0 (199 N/m) is similar to the forsterite one (197 N/m) according to Dauphas et al (2014). In this study, the initial value is replaced by the DFT force constant of forsterite (147 N/m) in order to correct for any method bias between our first-principles calculations and the NRIXS-derived data.

Two different models were performed in order to see the impact of Fe^{2+}-bearing silicates on iron isotope partitioning during magmatic differentiation: i) The first model applies a general $\alpha_{forsterite\text{-}melt}$ to represent the fractionation between the melt and all Fe^{2+}-bearing silicates as previously done in Dauphas et al. (2014) and, for rocks going up to ~65wt% SiO_2, Sossi et al. (2012). ii) The second model uses distinct fractionation factors for orthopyroxene and clinopyroxene $\alpha_{enstatite\text{-}melt}$ and $\alpha_{augite\text{-}melt}$. In order to be representative of the spinel composition along the magnetite-ulvospinel solid-solution, the $\alpha_{spinel\text{-}melt}$ is considered as a mixture of $\alpha_{ulvospinel\text{-}melt}$ and $\alpha_{magnetite\text{-}melt}$ in models 1 and 2. In order to

account for ilmenite crystallization during the last stage of magma differentiation (SiO_2 > 75 wt%), the ilmenite β-factor was calculated from the ilmenite Fe force constant of 137 N/m determined by Sossi and O'Neill (2017). A caveat with Dauphas et al. (2014) and this modeling (see Supplementary Tables) is that they involve clinopyroxene as the main phase producing Fe isotope fractionation, including at the granitic stage of magma evolution. However, this mineral is only an accessory mineral in granites, occurring especially in alkaline granites. It is possible though that clinopyroxene was subsequently transformed into amphibole and/or biotite at a late magmatic stage (Clemens et al., 1986).

Despite the mentioned approximation for the melt β-factor, the modeled iron isotopic evolution (Fig. 7), is consistent with the values of natural samples taken from the literature (Poitrasson and Freydier, 2005; Teng et al., 2008; Schuessler et al., 2009; Sossi et al., 2012; Zambardi et al., 2014; Foden et al., 2014; Williams et al., 2018) with a small increase of δ^{57}Fe from 0.1 to 0.15 ‰ up to 68% SiO_2 followed by a sharp increase up to 0.71 ‰ for model 1, and up to 0.98 ‰ for model 2 at 76 % SiO_2. Model 1 using a general fractionation factor for all Fe^{2+}-bearing minerals cannot reproduce the heaviest iron isotopic values (up to 0.93 ‰) at the last stage of differentiation whereas model 2 where α_{bulk} takes into account the nature of the pyroxenes can. As already underlined by Dauphas et al. (2014), fractional crystallization is probably responsible for the iron isotopic evolution of the magma toward heavy signatures during magmatic differentiation. The present results emphasize the importance of the distinct isotopic signatures of Fe^{2+}-bearing minerals such as pyroxenes during fractional crystallization (model 2 versus model 1).

In addition, we assumed here the same sigmoidal shape of the melt β-factor as in Dauphas et al. (2014). This is a critical parameter of the modeling that calls for a thorough investigation of the melt isotopic properties by first-principles molecular dynamics. Therefore, and although unknowns remain, such as the actual β factors of the evolving silicate melts, this modeling, involving new and self-consistent theoretical mineral Fe isotope fractionation factors to reduce the under-constrained nature of such multi-parametric modeling (Dauphas et al., 2017; Poitrasson et al., 2019), suggests that fractional crystallization is a viable way to interpret the global Fe isotope trend observed among terrestrial igneous rocks (Fig. 7).

CONCLUSION

Equilibrium iron and silicon isotope fractionation factors were calculated from first-principles methods in silicate and oxide minerals covering a wide range of minerals formed during magmatic differentiation. Significant isotopic fractionations are observed between the studied minerals even at high temperature. Our results allow us to conclude that Fe and Si isotope fractionations among Fe^{2+}-bearing minerals are not negligible in magmatic contexts. Among the parameters investigated, the results show that oxidation state and coordination number explain to a certain extent isotopic fractionation. Accordingly, Fe^{3+}-bearing minerals and minerals that have four-fold coordinated iron display higher force constants than Fe^{2+}-bearing minerals and minerals that have six-fold coordinated iron. However, this study allows to go a step further in showing that after temperature, the main parameter influencing the β-factors of minerals containing atomic species displaying similar coordination number and charge is the local crystal chemical environment. It can be described as the nature and number of the cations bound to the atom of interest.

This theoretical study of some of the main magmatic minerals provides a self-consistent set of fractionation factors to better assess the processes involved in isotopic fractionation during crust formation. As such, it could help to better understand the bulk Si and Fe isotopic compositions of igneous crustal rocks. Simple fractional crystallization models using our DFT-derived β-factors enabled us to underline the significant impact of the Fe^{2+}-bearing minerals on iron isotope fractionation during magmatic differentiation. However, in order to precisely quantify the impact of fractional crystallization on the Fe isotopic evolution of melts, it is essential to have the theoretical β-factors for different types of melt (e.g with various Fe^{3+}/Fe_{tot} ratios and with different cationic environment).

Acknowledgements:
We thank the associate editor Dr. Fang Huang and the two anonymous reviewers for their efforts to improve our manuscript. This work was supported by the ECOS-NORD/COLCIENCIAS French-Colombian cooperation program (Project number: C17U01). CP also acknowledges funding from MINCIENCIAS through research grants No. 2015-710-51568. This work was also supported through a grant to FP from the "Programme National de Planétologie-PNP" of CNRS/INSU, co-funded by CNES. Calculations were performed using the HPC resources from CALMIP (Grant 2019 – P1037). SR deeply thanks CALMIP staff for their support.

BIBLIOGRAPHY

Armytage R. M. G., Georg R. B., Williams H. M. and Halliday A. N. (2012) Silicon isotopes in lunar rocks: Implications for the Moon's formation and the early history of the Earth. *Geochim. Cosmochim. Acta* **77**, 504–514. Available at: http://dx.doi.org/10.1016/j.gca.2011.10.032.

Bader R. F. W. (2001) The zero-flux surface and the topological and quantum definitions of an atom in a molecule. *Theor. Chem. Acc.* **105**, 276–283. Available at: https://doi.org/10.1007/s002140000233.

Bader R. F. W. and Matta C. F. (2001) Properties of atoms in crystals: Dielectric polarization. *Int. J. Quantum Chem.* **85**, 592–607.

Barth T. F. W. and Posnjak E. (1932) Spinel structures: with and without variate atom equipoints. *Zeitschrift für Krist. - Cryst. Mater.* **82**, 325–341.

Baum E., Treutmann W., Lottermoser W. and Amthauer G. (1997) Magnetic properties of the clinopyroxenes aegirine and hedenbergite: A magnetic susceptibility study on single crystals. *Phys. Chem. Miner.* **24**, 294–300.

Beard B. L. and Johnson C. M. (2004) Inter-mineral Fe isotope variations in mantle-derived rocks and implications for the Fe geochemical cycle. *Geochim. Cosmochim. Acta* **68**, 4727–4743.

Bigeleisen J. and Mayer M. G. (1947) Calculation of Equilibrium Constants for Isotopic Exchange Reactions. *J. Chem. Phys.* **15**, 261–267. Available at: https://doi.org/10.1063/1.1746492.

Blanchard M., Ingrin J., Balan E., Kovács I. and Withers A. C. (2017) Effect of iron and trivalent cations

on OH defects in olivine. *Am. Mineral.* **102**, 302–311.

Blanchard M., Morin G., Lazzeri M., Balan E. and Dabo I. (2012) First-principles simulation of arsenate adsorption on the (1$\bar{1}$2) surface of hematite. *Geochim. Cosmochim. Acta* **86**, 182–195.

Blanchard M., Poitrasson F., Méheut M., Lazzeri M., Mauri F. and Balan E. (2009) Iron isotope fractionation between pyrite (FeS2), hematite (Fe2O3) and siderite (FeCO3): A first-principles density functional theory study. *Geochim. Cosmochim. Acta* **73**, 6565–6578.

Bohrson W. A., Spera F. J., Ghiorso M. S., Brown G. A., Creamer J. B. and Mayfield A. (2014) Thermodynamic model for energy-constrained open-system evolution of crustal magma bodies undergoing simultaneous recharge, assimilation and crystallization: The magma chamber simulator. *J. Petrol.* **55**, 1685–1717.

Bosi F., Hålenius U. and Skogby H. (2009) Crystal chemistry of the magnetite-ulvöspinel series. *Am. Mineral.* **94**, 181–189.

Böstrom Dan (1987) Single-crystal X-ray diffraction studies of synthetic Ni-Mg olivine solid solutions. *Am. Mineral.* **72**, 965–972.

Brown G. E. and Prewitt C. T. (1973) High-Temperature Crystal Chemistry of Hortonolite. *Am. Mineral.* **58**, 577–587.

Cameron M. and Papike J. J. (1981) Structural and chemical variations in pyroxenes. *Am. Mineral.* **66**, 1–50.

Cameron M., Sueno S., Prewitt C. T. and Papike J. J. (1973) High-Temperature crystal chemistry of acmite, diopside, hedenbergite, jadeite, spodumene, and Ureyite. *Am. Mineral.* **58**, 594–618.

Clark J. R., Appleman D. E. and Papike J. J. (1969) Crystal-Chemical Characterization of Clinopyroxenes Based on Eight New Structure Refinements. *Mineral. Soc. Am. - Spec. Pap.* **50**, 31–50.

Clemens, J.D., Holloway, J.R., White, A.J.R., 1986. Origin of an A-type granite: experimental constraints. American Mineralogist, 71: 317-324.

Cococcioni M., Dal Corso A. and de Gironcoli S. (2003) Structural, electronic, and magnetic properties of Fe2SiO4 fayalite: Comparison of LDA and GGA results. *Phys. Rev. B - Condens. Matter Mater. Phys.* **67**, 941061–941067.

Collinet M., Charlier B., Namur O., Oeser M., Médard E. and Weyer S. (2017) Crystallization history of enriched shergottites from Fe and Mg isotope fractionation in olivine megacrysts. *Geochim. Cosmochim. Acta* **207**, 277–297. Available at: http://dx.doi.org/10.1016/j.gca.2017.03.029.

Dauphas N. (2017) The isotopic nature of the Earth's accreting material through time. *Nature* **541**, 521–524. Available at: http://dx.doi.org/10.1038/nature20830.

Dauphas N., Roskosz M., Alp E. E., Golden D. C., Sio C. K., Tissot F. L. H., Hu M. Y., Zhao J., Gao L. and Morris R. V. (2012) A general moment NRIXS approach to the determination of equilibrium Fe isotopic fractionation factors: Application to goethite and jarosite. *Geochim. Cosmochim. Acta* **94**, 254–275.

Dauphas N., Roskosz M., Alp E. E., Neuville D. R., Hu M. Y., Sio C. K., Tissot F. L. H., Zhao J., Tissandier L., Médard E. and Cordier C. (2014) Magma redox and structural controls on iron isotope variations in Earth's mantle and crust. *Earth Planet. Sci. Lett.* **398**, 127–140.

Du D. H., Wang X. L., Yang T., Chen X., Li J. Y. and Li W. (2017) Origin of heavy Fe isotope compositions in high-silica igneous rocks: A rhyolite perspective. *Geochim. Cosmochim. Acta* **218**, 58–72. Available at: https://doi.org/10.1016/j.gca.2017.09.014.

Ducher M., Blanchard M. and Balan E. (2016) Equilibrium zinc isotope fractionation in Zn-bearing minerals from first-principles calculations. *Chem. Geol.* **443**, 87–96. Available at: http://dx.doi.org/10.1016/j.chemgeo.2016.09.016.

Foden J., Sossi P. A. and Wawryk C. M. (2015) Fe isotopes and the contrasting petrogenesis of A-, I- and S-type granite. *Lithos* **212–215**, 32–44. Available at: http://dx.doi.org/10.1016/j.lithos.2014.10.015.

Foden J., Sossi P. and Wawryk C. (2014) *Fe isotopes and the contrasting petrogenesis of A-, I- and S-type granite*.,

Gajos N. A., Lundstrom C. C. and Taylor A. H. (2016) Spatially controlled Fe and Si isotope variations: an alternative view on the formation of the Torres del Paine pluton. *Contrib. to Mineral. Petrol.*

171.

Garrity K. F., Bennett J. W., Rabe K. M. and Vanderbilt D. (2014) Pseudopotentials for high-throughput DFT calculations. *Comput. Mater. Sci.* **81**, 446–452. Available at: http://dx.doi.org/10.1016/j.commatsci.2013.08.053.

Gatta G. D., Bosi F., McIntyre G. J. and Hålenius U. (2014) Static positional disorder in ulvöspinel: A single-crystal neutron diffraction study. *Am. Mineral.* **99**, 255–260.

Georg R. B., Halliday A. N., Schauble E. A. and Reynolds B. C. (2007) Silicon in the Earth's core. *Nature* **447**, 1102–1106.

Giannozzi P., Baroni S., Bonini N., Calandra M., Car R., Cavazzoni C., Ceresoli D., Chiarotti G. L., Cococcioni M., Dabo I., Dal Corso A., De Gironcoli S., Fabris S., Fratesi G., Gebauer R., Gerstmann U., Gougoussis C., Kokalj A., Lazzeri M., Martin-Samos L., Marzari N., Mauri F., Mazzarello R., Paolini S., Pasquarello A., Paulatto L., Sbraccia C., Scandolo S., Sclauzero G., Seitsonen A. P., Smogunov A., Umari P. and Wentzcovitch R. M. (2009) QUANTUM ESPRESSO: A modular and open-source software project for quantum simulations of materials. *J. Phys. Condens. Matter* **21**.

Grant F. S. (1954) The geological significance of variations in the abundances of the isotopes of silicon in rocks. *Geochim. Cosmochim. Acta* **5**, 225–242. Available at: http://www.sciencedirect.com/science/article/pii/0016703754900460.

De Grave E. and Van Alboom A. (1991) Evaluation of ferrous and ferric Mössbauer fractions. *Phys. Chem. Miner.* **18**, 337–342. Available at: https://doi.org/10.1007/BF00200191.

De Grave E., Persoons R. M., Vandenberghe R. E. and De Bakker P. M. A. (1993) Mössbauer study of the high-temperature phase of Co-substituted magnetites, CoxFe3-xO4. I. x0.04. *Phys. Rev. B* **47**, 5881–5893.

Georg R. B., Halliday A. N., Schauble E. A. and Reynolds B. C. (2007) Silicon in the Earth's core. *Nature* **447**, 1102–1106. Available at: https://doi.org/10.1038/nature05927.

Gualda G. A. R., Ghiorso M. S., Lemons R. V and Carley T. L. (2012) Rhyolite-MELTS: a Modified Calibration of MELTS Optimized for Silica-rich, Fluid-bearing Magmatic Systems. *J. Petrol.* **53**, 875–890. Available at: https://doi.org/10.1093/petrology/egr080.

Haavik C., Stølen S., Fjellvåg H., Hanfland M. and Häusermann D. (2000) Equation of state of magnetite and its high-pressure modification: Thermodynamics of the Fe-O system at high pressure. *Am. Mineral.* **85**, 514–523.

He Y., Wu H., Ke S., Liu S. A. and Wang Q. (2017) Iron isotopic compositions of adakitic and non-adakitic granitic magmas: Magma compositional control and subtle residual garnet effect. *Geochim. Cosmochim. Acta* **203**, 89–102. Available at: http://dx.doi.org/10.1016/j.gca.2017.01.005.

Henkelman G., Arnaldsson A. and Jónsson H. (2006) A fast and robust algorithm for Bader decomposition of charge density. *Comput. Mater. Sci.* **36**, 354–360.

Hexiong Yang and Subratra Ghose (1995) A transitional structural state and anomalous Fe-Mg order-disorder in Mg-rich orthopyroxene, (Mg0.75Fe0.25)2Si2O6. *Am. Mineral.* **80**, 9–20.

Huang F., Wu Z., Huang S. and Wu F. (2014) First-principles calculations of equilibrium silicon isotope fractionation among mantle minerals. *Geochim. Cosmochim. Acta* **140**, 509–520. Available at: http://dx.doi.org/10.1016/j.gca.2014.05.035.

Javoy M., Balan E., Méheut M., Blanchard M. and Lazzeri M. (2012) First-principles investigation of equilibrium isotopic fractionation of O- and Si-isotopes between refractory solids and gases in the solar nebula. *Earth Planet. Sci. Lett.* **319–320**, 118–127. Available at: http://dx.doi.org/10.1016/j.epsl.2011.12.029.

Kunz M. and David Brown I. (1995) Out-of-center distortions around octahedrally coordinated d0 transition metals. *J. Solid State Chem.* **115**, 395–406.

Li Q. W., Zhao J. H., Wang Q., Zhang Z. F., An Y. J. and He Y. T. (2020) Iron isotope fractionation in hydrous basaltic magmas in deep crustal hot zones. *Geochim. Cosmochim. Acta* **279**, 29–44. Available at: https://doi.org/10.1016/j.gca.2020.03.032.

Lundstrom C. (2009) Hypothesis for the origin of convergent margin granitoids and Earth's

continental crust by thermal migration zone refining. *Geochim. Cosmochim. Acta* **73**, 5709–5729. Available at: https://www.sciencedirect.com/science/article/pii/S0016703709004116 [Accessed April 26, 2019].

McCammon C. and Kopylova M. G. (2004) A redox profile of the Slave mantle and oxygen fugacity control in the cratonic mantle. *Contrib. to Mineral. Petrol.* **148**, 55–68.

McCarty R. J., Palke A. C., Stebbins J. F. and Hartman S. (2015) Transition metal cation site preferences in forsterite (Mg2SiO4) determined from paramagnetically shifted NMR resonances. *Am. Mineral.* **100**, 1265–1276.

Méheut M., Lazzeri M., Balan E. and Mauri F. (2009) Structural control over equilibrium silicon and oxygen isotopic fractionation: A first-principles density-functional theory study. *Chem. Geol.* **258**, 28–37. Available at: http://dx.doi.org/10.1016/j.chemgeo.2008.06.051.

Méheut M. and Schauble E. A. (2014) Silicon isotope fractionation in silicate minerals: Insights from first-principles models of phyllosilicates, albite and pyrope. *Geochim. Cosmochim. Acta* **134**, 137–154. Available at: http://dx.doi.org/10.1016/j.gca.2014.02.014.

Mineev S. D., Polyakov V. B. and Permyakov Y. V. (2007) Equilibrium iron isotope fractionation factors for magnetite from Mössbauer spectroscopy and inelastic nuclear resonant X-ray scattering data. *Geochim. Cosmochim. Acta* **71 (Suppl)**.

Monkhorst H. J. and Pack J. D. (1976) Special points for Brillouin-zone integrations. *Phys. Rev. B* **13**, 5188–5192. Available at: https://link.aps.org/doi/10.1103/PhysRevB.13.5188.

Nebel O., Sossi P. A., Bénard A., Wille M., Vroon P. Z. and Arculus R. J. (2015) Redox-variability and controls in subduction zones from an iron-isotope perspective. *Earth Planet. Sci. Lett.* **432**.

Oeser M., Dohmen R., Horn I., Schuth S. and Weyer S. (2015) Processes and time scales of magmatic evolution as revealed by Fe-Mg chemical and isotopic zoning in natural olivines. *Geochim. Cosmochim. Acta* **154**, 130–150. Available at: http://dx.doi.org/10.1016/j.gca.2015.01.025.

Oeser M., Ruprecht P. and Weyer S. (2018) Combined Fe-Mg chemical and isotopic zoning in olivine constraining magma mixing-to-eruption timescales for the continental arc volcano Irazú (Costa Rica) and Cr diffusion in olivine. *Am. Mineral.* **103**, 582–599.

Oeser M., Weyer S., Horn I. and Schuth S. (2014) High-precision fe and mg isotope ratios of silicate reference glasses determined in situ by femtosecond LA-MC-ICP-MS and by solution nebulisation MC-ICP-MS. *Geostand. Geoanalytical Res.* **38**, 311–328.

Pack A., Vogel I., Rollion-Bard C., Luais B. and Palme H. (2011) Silicon in iron meteorite metal. *Meteorit. Planet. Sci.* **46**, 1470–1483. Available at: https://onlinelibrary.wiley.com/doi/abs/10.1111/j.1945-5100.2011.01239.x.

Perdew J. P., Burke K. and Ernzerhof M. (1996) Generalized gradient approximation made simple. *Phys. Rev. Lett.* **77**, 3865–3868.

Poitrasson F. (2017) Silicon Isotope Geochemistry. *Rev. Mineral. Geochemistry* **82**, 289–344. Available at: https://doi.org/10.2138/rmg.2017.82.8.

Poitrasson F. and Freydier R. (2005) Heavy iron isotope composition of granites determined by high resolution MC-ICP-MS. *Chem. Geol.* **222**, 132–147. Available at: https://linkinghub.elsevier.com/retrieve/pii/S0009254105002615.

Poitrasson F. and Zambardi T. (2015) An Earth-Moon silicon isotope model to track silicic magma origins. *Geochim. Cosmochim. Acta* **167**, 301–312. Available at: http://dx.doi.org/10.1016/j.gca.2015.07.005.

Poitrasson F., Zambardi T., Magna T. and Neal C. R. (2019) A reassessment of the iron isotope composition of the Moon and its implications for the accretion and differentiation of terrestrial planets. *Geochim. Cosmochim. Acta* **267**, 257–274. Available at: https://doi.org/10.1016/j.gca.2019.09.035.

Polyakov V. B. (2009) Equilibrium iron isotope fractionation at core-mantle boundary conditions. *Science (80-.).* **323**, 912–914.

Polyakov V. B., Clayton R. N., Horita J. and Mineev S. D. (2007) Equilibrium iron isotope fractionation factors of minerals: Reevaluation from the data of nuclear inelastic resonant X-ray scattering and Mössbauer spectroscopy. *Geochim. Cosmochim. Acta* **71**, 3833–3846.

Polyakov V. B. and Mineev S. D. (2000) The use of Mossbauer spectroscopy in stable isotope geochemistry. *Geochim. Cosmochim. Acta* **64**, 849–865.

Polyakov V. B., Osadchii E. G., Voronin M. V., Osadchii V. O., Sipavina L. V., Chareev D. A., Tyurin A. V., Gurevich V. M. and Gavrichev K. S. (2019) Iron and Sulfur Isotope Factors of Pyrite: Data from Experimental Mössbauer Spectroscopy and Heat Capacity. *Geochemistry Int.* **57**, 369–383.

Polyakov V. B. and Soultanov D. M. (2011) New data on equilibrium iron isotope fractionation among sulfides: Constraints on mechanisms of sulfide formation in hydrothermal and igneous systems. *Geochim. Cosmochim. Acta* **75**, 1957–1974. Available at: http://dx.doi.org/10.1016/j.gca.2011.01.019.

Polyakov V., Osadchii E., Chareev D., Chumakov A. and Sergueev I. (2013) Fe β-Factors for Sulfides from NRIXS Synchrotron Experiments. *Miner. Mag.* **77**.

Pringle E. A., Moynier F., Savage P. S., Badro J. and Barrat J. A. (2014) Silicon isotopes in angrites and volatile loss in planetesimals. *Proc. Natl. Acad. Sci. U. S. A.* **111**, 17029–17032.

Prissel K. B., Krawczynski M. J., Nie N. X., Dauphas N., Couvy H., Hu M. Y., Alp E. E. and Roskosz M. (2018) Experimentally determined effects of olivine crystallization and melt titanium content on iron isotopic fractionation in planetary basalts. *Geochim. Cosmochim. Acta* **238**, 580–598.

Qin T., Wu F., Wu Z. and Huang F. (2016) First-principles calculations of equilibrium fractionation of O and Si isotopes in quartz, albite, anorthite, and zircon. *Contrib. to Mineral. Petrol.* **171**.

Redhammer G. J., Amthauer G., Roth G., Tippelt G. and Lottermoser W. (2006) Single-crystal X-ray diffraction and temperature dependent 57Fe Mössbauer spectroscopy on the hedenbergite-aegirine (Ca,Na)(Fe2+,Fe3+)Si2O6 solid solution. *Am. Mineral.* **91**, 1271–1292.

Roskosz M., Sio C. K. I., Dauphas N., Bi W., Tissot F. L. H., Hu M. Y., Zhao J. and Alp E. E. (2015) Spinel-olivine-pyroxene equilibrium iron isotopic fractionation and applications to natural peridotites. *Geochim. Cosmochim. Acta* **169**, 184–199.

Savage P. S., Georg R. B., Armytage R. M. G., Williams H. M. and Halliday A. N. (2010) Silicon isotope homogeneity in the mantle. *Earth Planet. Sci. Lett.* **295**, 139–146. Available at: http://dx.doi.org/10.1016/j.epsl.2010.03.035.

Savage P. S., Georg R. B., Williams H. M., Burton K. W. and Halliday A. N. (2011) Silicon isotope fractionation during magmatic differentiation. *Geochim. Cosmochim. Acta* **75**, 6124–6139. Available at: http://dx.doi.org/10.1016/j.gca.2011.07.043.

Schoenberg R., Marks M. A. W., Schuessler J. A., von Blanckenburg F. and Markl G. (2009) Fe isotope systematics of coexisting amphibole and pyroxene in the alkaline igneous rock suite of the Ilímaussaq Complex, South Greenland. *Chem. Geol.* **258**, 65–77. Available at: https://www.sciencedirect.com/science/article/pii/S0009254108002416 [Accessed April 26, 2019].

Schuessler J. A., Schoenberg R. and Sigmarsson O. (2009) Iron and lithium isotope systematics of the Hekla volcano, Iceland - Evidence for Fe isotope fractionation during magma differentiation. *Chem. Geol.* **258**, 78–91. Available at: http://dx.doi.org/10.1016/j.chemgeo.2008.06.021.

Shahar A., Hillgren V. J., Young E. D., Fei Y., Macris C. A. and Deng L. (2011) High-temperature Si isotope fractionation between iron metal and silicate. *Geochim. Cosmochim. Acta* **75**, 7688–7697.

Shahar A., Young E. D. and Manning C. E. (2008) Equilibrium high-temperature Fe isotope fractionation between fayalite and magnetite: An experimental calibration. *Earth Planet. Sci. Lett.* **268**, 330–338. Available at: https://www.sciencedirect.com/science/article/pii/S0012821X08000435 [Accessed April 26, 2019].

Sio C. K. I., Dauphas N., Teng F. Z., Chaussidon M., Helz R. T. and Roskosz M. (2013) Discerning crystal growth from diffusion profiles in zoned olivine by in situ Mg-Fe isotopic analyses. *Geochim. Cosmochim. Acta* **123**, 302–321. Available at: http://dx.doi.org/10.1016/j.gca.2013.06.008.

Smyth J. R. (1975) High Temperature Crystal Chemistry of Fayalite. *Am. Mineral.* **60**, 1092–1097.

Sossi P. A., Foden J. D. and Halverson G. P. (2012) Redox-controlled iron isotope fractionation during magmatic differentiation: An example from the Red Hill intrusion, S. Tasmania. *Contrib. to*

Mineral. Petrol. **164**, 757–772.

Sossi P. A. and O'Neill H. S. C. (2017) The effect of bonding environment on iron isotope fractionation between minerals at high temperature. *Geochim. Cosmochim. Acta* **196**, 121–143. Available at: https://www.sciencedirect.com/science/article/pii/S0016703716305324 [Accessed April 26, 2019].

Telus M., Dauphas N., Moynier F., Tissot F. L. H., Teng F. Z., Nabelek P. I., Craddock P. R. and Groat L. A. (2012) Iron, zinc, magnesium and uranium isotopic fractionation during continental crust differentiation: The tale from migmatites, granitoids, and pegmatites. *Geochim. Cosmochim. Acta* **97**, 247–265.

Teng F.-Z., Dauphas N. and Helz R. T. (2008) Iron Isotope Fractionation During Magmatic Differentiation in Kilauea Iki Lava Lake. *Science (80-.).* **320**, 1620–1622. Available at: http://science.sciencemag.org/content/320/5883/1620.abstract.

Teng F. Z., Dauphas N., Helz R. T., Gao S. and Huang S. (2011) Diffusion-driven magnesium and iron isotope fractionation in Hawaiian olivine. *Earth Planet. Sci. Lett.* **308**, 317–324. Available at: http://dx.doi.org/10.1016/j.epsl.2011.06.003.

Teng F. Z., Dauphas N., Huang S. and Marty B. (2013) Iron isotopic systematics of oceanic basalts. *Geochim. Cosmochim. Acta* **107**, 12–26. Available at: http://dx.doi.org/10.1016/j.gca.2012.12.027.

Umemoto K., Wentzcovitch R. M., Hirschmann M. M., Kohlstedt D. L. and Withers A. C. (2011) A first-principles investigation of hydrous defects and IR frequencies in forsterite: The case for Si vacancies. *Am. Mineral.* **96**, 1475–1479.

Wai C. M. and Wasson J. T. (1969) Silicon concentrations in the metal of iron meteorites. *Geochim. Cosmochim. Acta* **33**, 1465–1471. Available at: http://www.sciencedirect.com/science/article/pii/0016703769901501.

Wang W., Zhou C., Qin T., Kang J. T., Huang S., Wu Z. and Huang F. (2017) Effect of Ca content on equilibrium Ca isotope fractionation between orthopyroxene and clinopyroxene. *Geochim. Cosmochim. Acta* **219**, 44–56. Available at: https://doi.org/10.1016/j.gca.2017.09.022.

Weyer S., Anbar A. D., Brey G. P., Münker C., Mezger K. and Woodland A. B. (2005) Iron isotope fractionation during planetary differentiation. *Earth Planet. Sci. Lett.* **240**, 251–264.

Weyer S. and Ionov D. A. (2007) Partial melting and melt percolation in the mantle: The message from Fe isotopes. *Earth Planet. Sci. Lett.* **259**, 119–133.

Williams H. M., McCammon C. A., Peslier A. H., Halliday A. N., Teutsch N., Levasseur S. and Burg J.-P. (2004) Iron Isotope Fractionation and the Oxygen Fugacity of the Mantle. *Science (80-.).* **304**, 1656 LP – 1659. Available at: http://science.sciencemag.org/content/304/5677/1656.abstract.

Williams H. M., Nielsen S. G., Renac C., Griffin W. L., O'Reilly S. Y., McCammon C. A., Pearson N., Viljoen F., Alt J. C. and Halliday A. N. (2009) Fractionation of oxygen and iron isotopes by partial melting processes: Implications for the interpretation of stable isotope signatures in mafic rocks. *Earth Planet. Sci. Lett.* **283**, 156–166. Available at: https://www.sciencedirect.com/science/article/pii/S0012821X0900226X [Accessed April 26, 2019].

Williams H. M., Peslier A. H., McCammon C., Halliday A. N., Levasseur S., Teutsch N. and Burg J. P. (2005) Systematic iron isotope variations in mantle rocks and minerals: The effects of partial melting and oxygen fugacity. *Earth Planet. Sci. Lett.* **235**, 435–452.

Williams H. M., Prytulak J., Woodhead J. D., Kelley K. A., Brounce M. and Plank T. (2018) Interplay of crystal fractionation, sulfide saturation and oxygen fugacity on the iron isotope composition of arc lavas: An example from the Marianas. *Geochim. Cosmochim. Acta* **226**, 224–243.

Woodland A. B. and Koch M. (2003) Variation in oxygen fugacity with depth in the upper mantle beneath the Kaapvaal craton, Southern Africa. *Earth Planet. Sci. Lett.* **214**, 295–310.

Wright J. P., Paul Attfield J. and Radaelli P. G. (2002) Charge ordered structure of magnetite (formula presented) below the Verwey transition. *Phys. Rev. B - Condens. Matter Mater. Phys.* **66**, 1–15.

Xia Y., Li S. and Huang F. (2017) Iron and Zinc isotope fractionation during magmatism in the continental crust: Evidence from bimodal volcanic rocks from Hailar basin, NE China. *Geochim.*

Cosmochim. Acta **213**, 35–46. Available at: http://dx.doi.org/10.1016/j.gca.2017.06.018.

Yaxley G. M., Berry A. J., Kamenetsky V. S., Woodland A. B. and Golovin A. V. (2012) An oxygen fugacity profile through the Siberian Craton - Fe K-edge XANES determinations of Fe 3+/∑Fe in garnets in peridotite xenoliths from the Udachnaya East kimberlite. *Lithos* **140–141**, 142–151. Available at: http://dx.doi.org/10.1016/j.lithos.2012.01.016.

Young E. D., Tonui E., Manning C. E., Schauble E. and Macris C. A. (2009) Spinel-olivine magnesium isotope thermometry in the mantle and implications for the Mg isotopic composition of Earth. *Earth Planet. Sci. Lett.* **288**, 524–533. Available at: http://dx.doi.org/10.1016/j.epsl.2009.10.014.

Zambardi, T., Poitrasson, F., Corgne, A., Meheut, M., Quitte, G., Anand, M., 2013. Silicon isotope variations in the inner solar system: Implications for planetary formation, differentiation and composition. Geochimica et Cosmochimica Acta, 121: 67-83.

Zambardi T., Lundstrom C. C., Li X. and McCurry M. (2014) Fe and Si isotope variations at Cedar Butte volcano; insight into magmatic differentiation. *Earth Planet. Sci. Lett.* **405**, 169–179. Available at: http://dx.doi.org/10.1016/j.epsl.2014.08.020.

Zhang L., Ahsbahs H., Hafner S. S. and Kutoglu A. (1997) Single-crystal compression and crystal structure of clinopyroxene up to 10 GPa. *Am. Mineral.* **82**, 245–258.

Zhu X. K., Guo Y., Williams R. J. P., O'Nions R. K., Matthews A., Belshaw N. S., Canters G. W., de Waal E. C., Weser U., Burgess B. K. and Salvato B. (2002) Mass fractionation processes of transition metal isotopes. *Earth Planet. Sci. Lett.* **200**, 47–62.

Ziegler K., Young E. D., Schauble E. A. and Wasson J. T. (2010) Metal-silicate silicon isotope fractionation in enstatite meteorites and constraints on Earth's core formation. *Earth Planet. Sci. Lett.* **295**, 487–496.

	Formula	sym	This study	Exp.	Space group	k-space
Enstatite	$Fe_2Mg_{14}Si_{16}O_{48}$	o	a= 18.456 b= 8.994 c= 5.273	a[1]= 18.2747(21) b[1]= 8.8729(9) c[1]= 5.1988(5)	Pbca	4x4x4
Ulvospinel	$Fe_{16}Ti_8O_{32}$	c	a= 8.483	a[2]= 8.4875(4)	Fd3m	2x2x2
Aegirine	$Fe_4Na_4Si_8O_{24}$	m	a= 9.857 b= 8.927 c= 5.368 γ= 107.764	a[3]= 9.7412(8) b[3]= 8.9086(7) c[3]= 5.2776(5) γ[3]= 106.221(5)	C 2/c	4x4x4
Augite	$(Ca_2Fe_2)(MgFe_3)Si_8O_{24}$	m	a= 10.007 b= 9.108 c= 5.284 γ= 107.525	a[4]= 9.699(1) b[4]= 8.884(1) c[4]= 5.272(1) γ[4]= 106.97(2)	C 2/c	4x4x4
Diospide	$Ca_4(FeMg_3)Si_8O_{24}$	m	a= 9.909 b= 9.051 c= 5.330 γ= 106.211	a[5]= 9.749(2) b[5]= 8.922(1) c[5]= 5.248(8) γ[5]= 106.04(1)	C 2/c	4x4x4
Hedenbergite	$Fe_4Ca_4Si_8O_{24}$	m	a= 10.039 b= 8.986 c= 5.251 γ= 104.14	a[5]= 9.838(2) b[5]= 9.021(7) c[5]= 5.242(7) γ[5]= 104.797(8)	C 2/c	4x4x4
Forsterite	$Fe_1Mg_7Si_4O_{16}$	o	a= 4.818 b= 10.366 c= 6.042	a[6]= 4.755(3) b[6]= 10.198(6) c[6]= 5.979(4)	Pnma	2x2x2
Forsterite	$Mg_8Si_4O_{16}$	o	a= 4.803 b= 10.328 c= 6.046	a[6]= 4.755(3) b[6]= 10.1985(6) c[6]= 5.9792(4)	Pnma	2x2x2
Hortonolite	$Fe_4Mg_4Si_4O_{16}$	o	a= 4.874 b= 10.443 c= 5.986	a[7]= 4.775(1) b[7]= 10.280(1) c[7]= 6.016(1)	Pnma	2x2x2
Fayalite	$Fe_8Si_4O_{16}$	o	a= 4.957 b= 10.411 c= 5.943	a[8]= 4.818(2) b[8]= 10.471(3) c[8]= 6.086(2)	Pnma	2x2x2
Magnetite	Fe_6O_8	c	a= 8.400	a[9]= 8.397	Fd3m	6x6x6

Table 1- Calculated and experimental lattice parameters (in Å) and space group of the studied minerals as well as the modeling parameters used in Quantum Espresso. c, o and m stand for cubic, orthorhombic and monoclinic crystal systems. References for the experimental lattice parameters are: 1 - Yang and Ghose, 1995*; 2 -* Bosi et al., 2009*; 3 - Redhammer et al., 2006; 4 - Clark et al., 1969; 5 -Zhang et al., 1997; 6 - Böstrom Dan, 1987; 7 -Brown and Prewitt, 1973; 8 - Smyth, 1975; 9- Haavik et al., 2000. Uncertainties are in brackets at the end of each experimental lattice parameters.*

	^{57}Fe / ^{54}Fe			^{30}Si / ^{28}Si			
	B1	B2	<F>	A	B	C	<F>
Aegirine	-0.0041	0.9226	216.4	0.0025	-0.1329	6.7378	647.8
Enstatite	-0.0028	0.6419	150.5	0.0029	-0.1484	7.0713	680.5

Forsterite M_1	-0.0021	0.6252	146.4	0.0028	-0.1490	7.1365	686.4
Augite	-0.0019	0.5459	127.8	0.0026	-0.1379	6.8474	658.5
Hortonolite	-0.0018	0.5661	134.3	0.0025	-0.1356	6.7722	650.9
Hedenbergite	-0.0014	0.5403	126.4	0.0026	-0.1389	6.8081	654.9
Forsterite M_2	-0.0016	0.5345	125.1	0.0028	-0.1501	7.1628	689.0
Fayalite	-0.0011	0.4258	99.6	0.0021	-0.1191	6.3368	608.6
Diopside	-0.0018	0.5803	135.9	0.0028	-0.1455	6.9465	668.5
Ulvospinel	-0.0023	0.6505	151.8				
Magnetite	-0.0032	0.8870	207.5				
Forsterite_Mg				0.0029	-0.1546	7.2781	700.2

Table 2-Polynomial fits of the reduced partition function ratios of $^{57}Fe/^{54}Fe$ and $^{30}Si/^{28}Si$ and average force constants, <F> in N/m. Polynomial fits use equation of type $B1x^2 + B2x$ for $10^3 ln\beta\ ^{57}Fe\text{-}^{54}Fe$ and $Ax^3 + Bx^2 + Cx$ for $10^3 ln\beta\ ^{30}Si\text{-}^{28}Si$ with $x = 10^6/T^2$ for T between 0 and 1500 K.

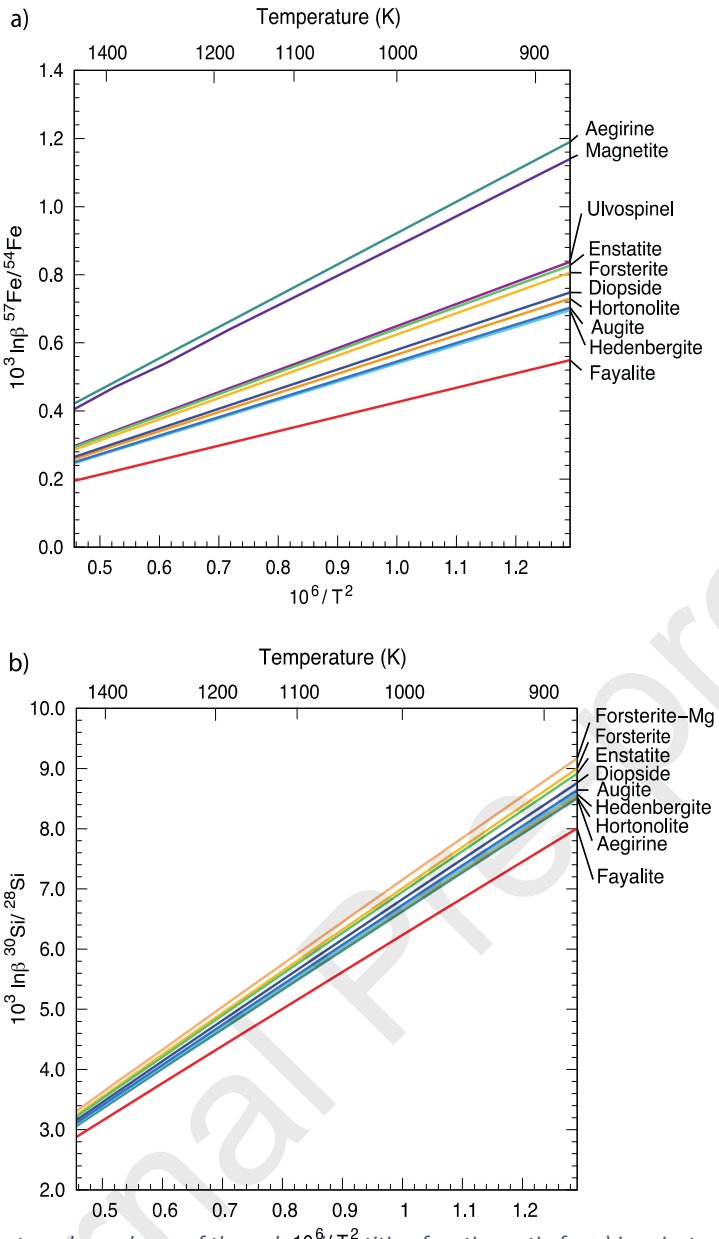

Figure 1- High temperature dependence of the reduced partition function ratio for a) iron isotopes and b) silicon isotopes. For clarity, only forsterite with iron in M_1 site is displayed in these figures.

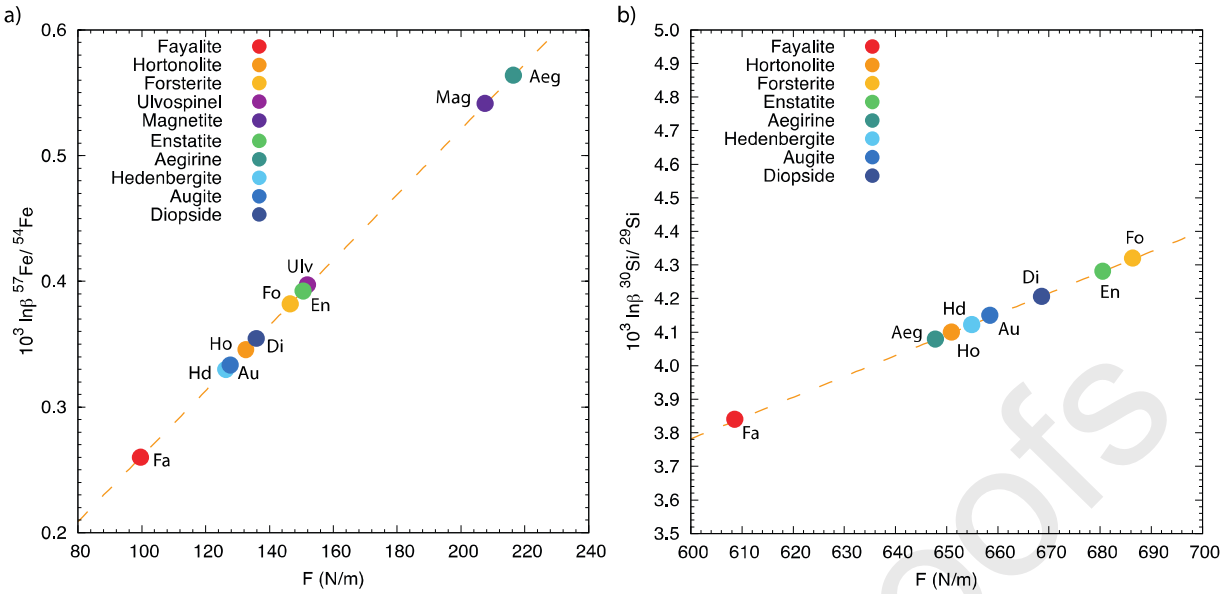

Figure 2- $10^3 ln\beta$ as a function of the average force constant for iron (a) and silicon (b) at T =1280 K. The linear fit between $10^3 ln\beta$ $^{57}Fe/^{54}Fe$ and the iron force constant is : f(x) = 0.0026x and is in total agreement with the equation of Dauphas et al. (2014). The linear fit between $10^3 ln\beta$ $^{30}Si/^{29}Si$ and the silicon force constant is: f(x) = 0.0062x.

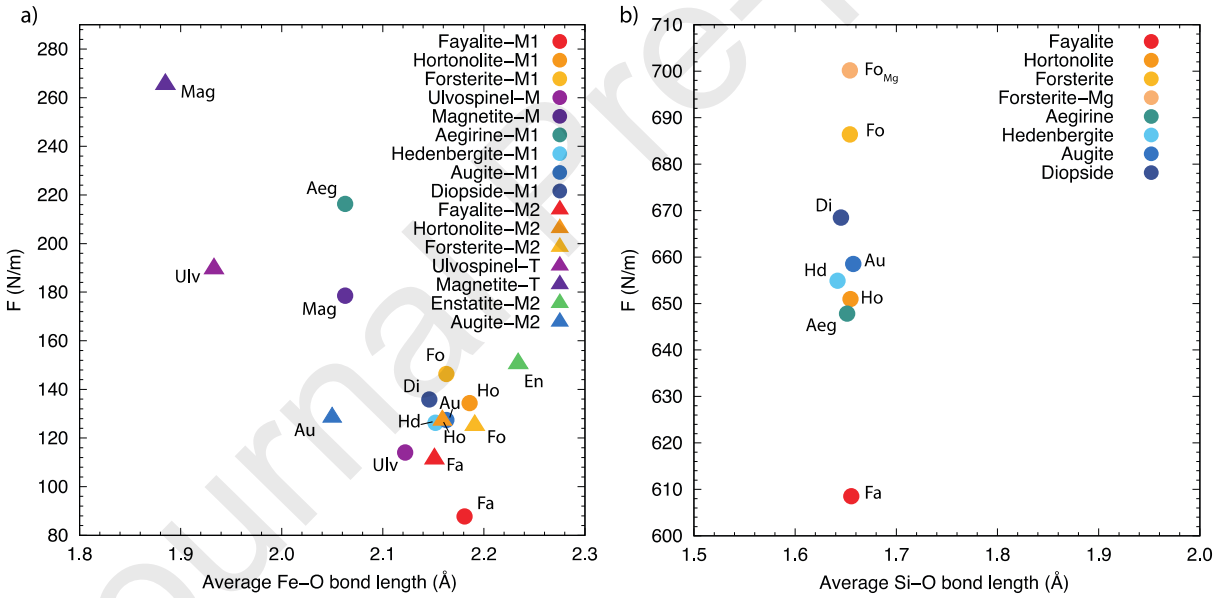

Figure 3-Relationship between the average force constants and the average bond lengths for Fe (a) and Si (b).

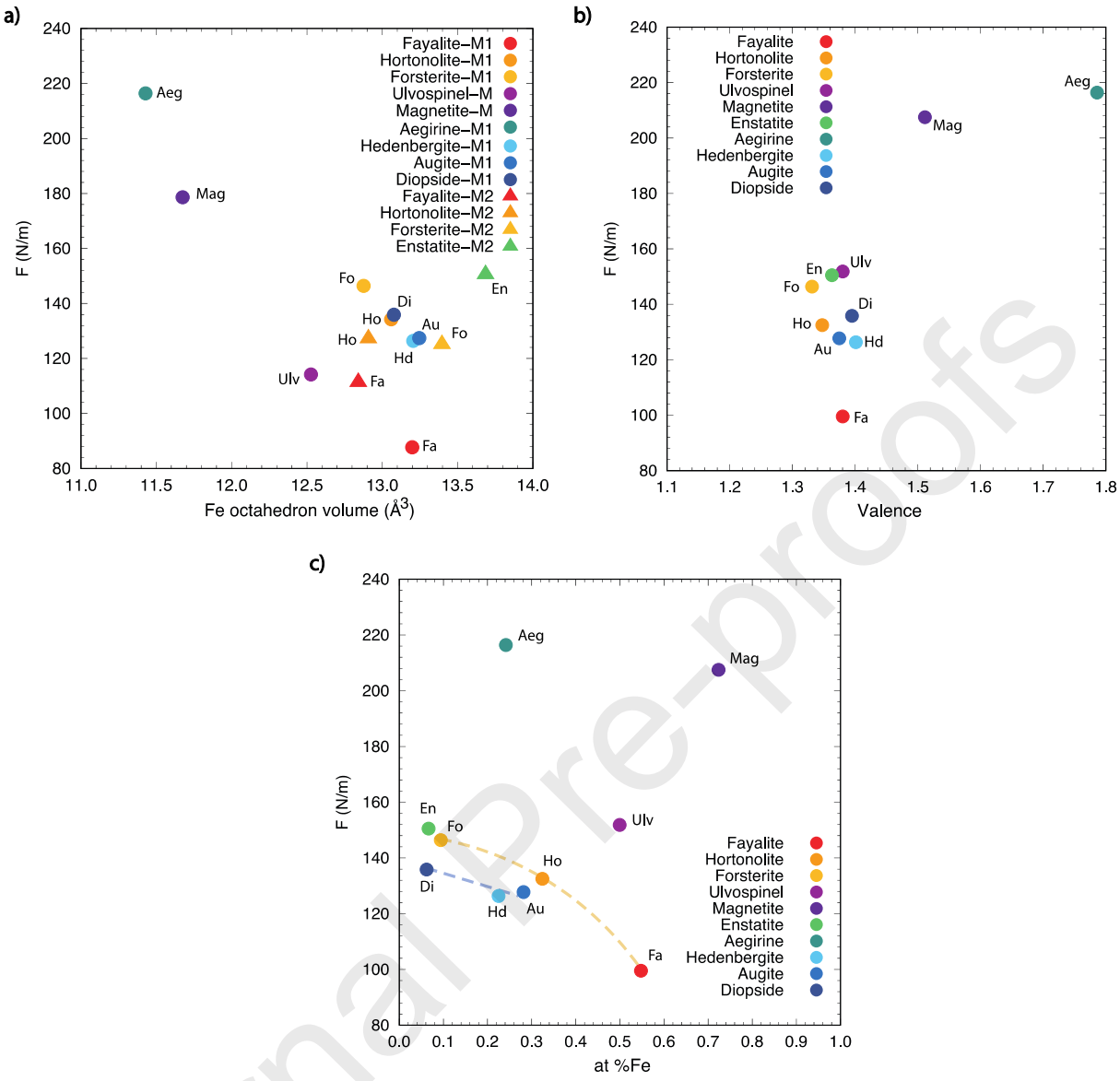

Figure 2- Iron force constant as a function of three parameters: a) Volume of the Fe octahedron, b) iron valence as given by the Bader charges (Henkelman et al., 2006) and c) iron concentration in the minerals. Dashed lines are only guides for the eye.

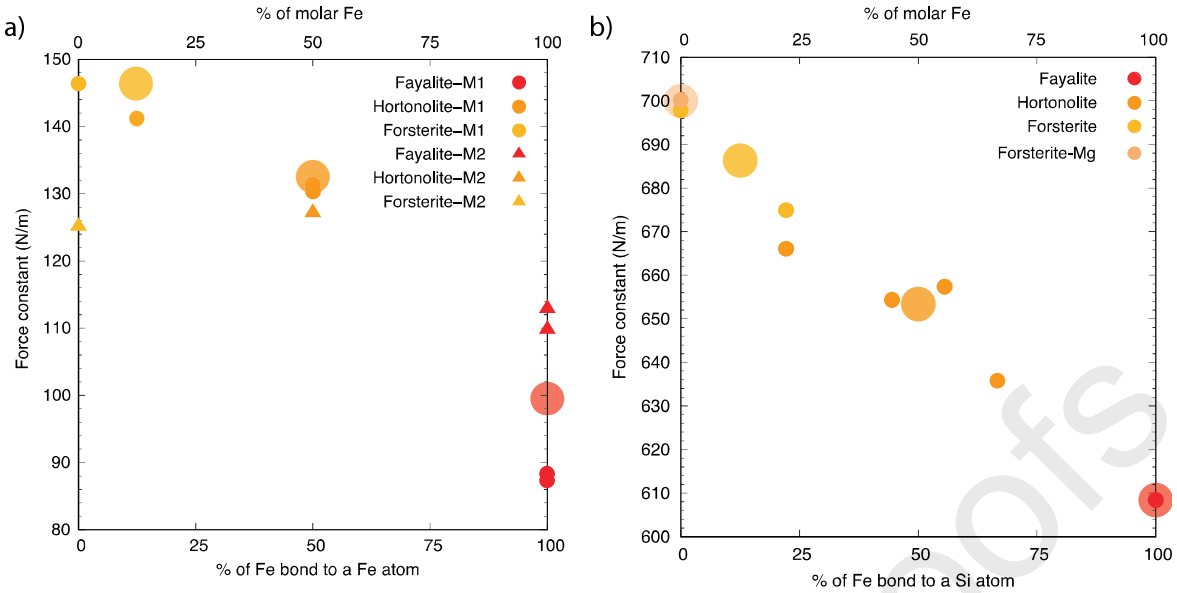

Figure 3- Evolution of the Fe (a) and Si (b) force constant in the olivine solid-solution as a function of the number of iron atoms in the neighboring crystal sites sharing an edge or a corner with the central Fe or Si polyhedron (small symbols for M1, M2 or Si sites, referring to the lower axis). For comparison, large circles correspond to the mean force constant evolution with the Fe molar concentration in the mineral M sites (upper axis). For example, in panel a, fayalite (red large circle) contains only iron and no magnesium in its M1 and M2 sites. Therefore, the corresponding iron concentration in M sites is 100 mol% Fe, and the mean Fe force constant (F = 99.6 N/m) is an average of the Fe force constants of the four Fe atoms in M1 sites (88.1, 88.3, 87.3 and 87.3 N/m) and of the four Fe atoms in M2 sites (109.8, 109.8, 112.9 and 112.9 N/m).

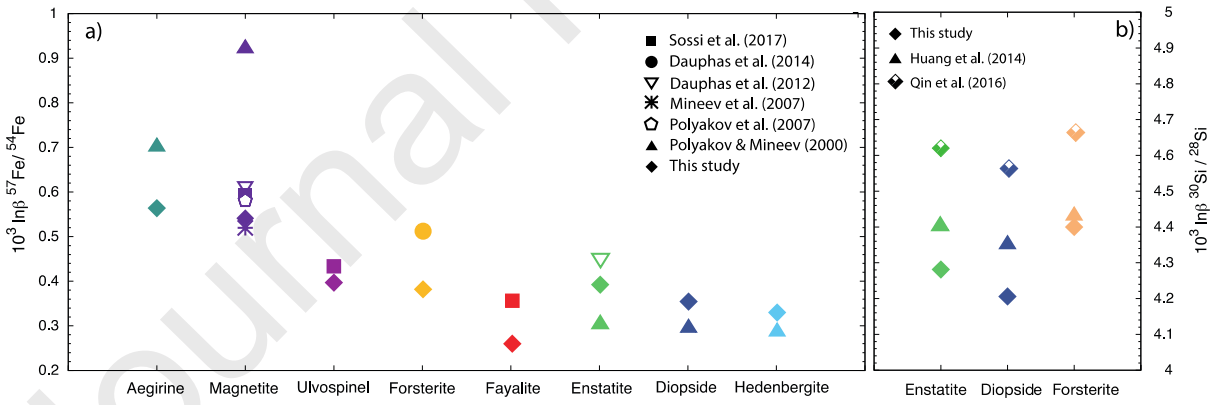

Figure 4- Comparison of the $10^3 \ln\beta\ ^{57}Fe/^{54}Fe$ (a) and $10^3 \ln\beta\ ^{30}Si/^{28}Si$ (b) calculated in the present study at T = 1280 K, with previous data computed from NRIXS measurements (Dauphas et al., 2012; Dauphas et al., 2014; *Polyakov et al. 2007; Mineev et al. 2007*), *Mössbauer spectroscopy (Polyakov and Mineev, 2000), experimental petrology (Sossi and Foden, 2017), and DFT calculations (Huang et al., 2014, Qin et al. 2016). The uncertainties are ≤ 0.05 ‰ for NRIXS-derived data (Dauphas et al., 2014, 2012; Polyakov et al. 2007, Mineev et al. 2007) and ≤ 0.10 ‰ for Mössbauer-derived data (Polyakov and Mineev, 2000).*

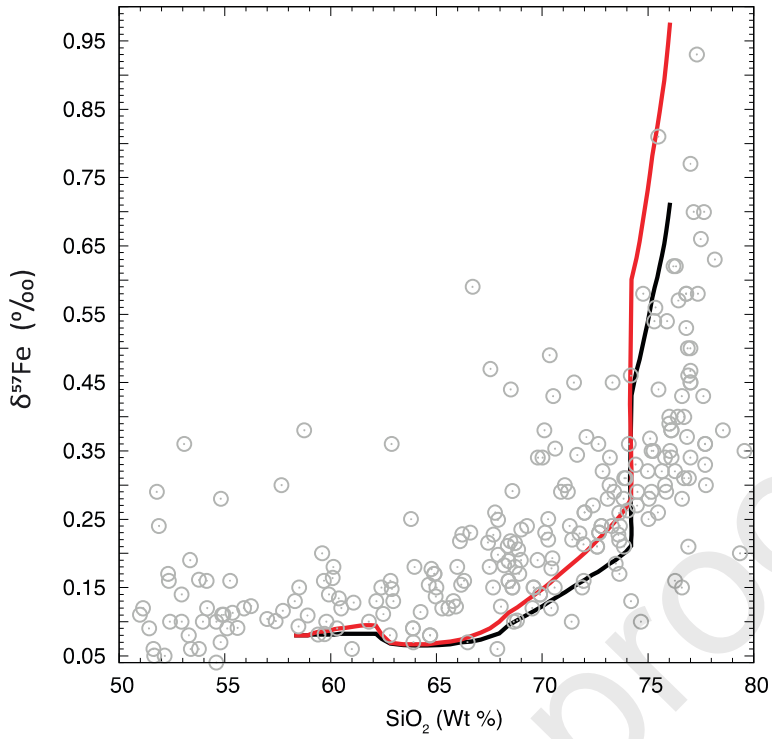

Figure 7 - Models of $\delta^{57}Fe$ evolution during magmatic differentiation: the black line represents model 1 where a bulk fractionation factor $\alpha_{forsterite\text{-}melt}$ is used with forsterite representing all Fe^{2+}-bearing minerals, and the red line represents model 2 where the differences between the relevant Fe^{2+}-bearing minerals are taken into account (i.e., $\alpha_{enstatite\text{-}melt}$, $\alpha_{augite\text{-}melt}$). Models were obtained using the MCS software (Bohrson and Spera, 2007) with starting andesite composition (SiO_2= 58.23, TiO_2 = 0.94, Al_2O_3 = 16.94, Cr_2O_3= 0.03, FeO = 7.31, MgO = 3.99, CaO = 7.08, Na_2O = 3.47, K_2O=1.57, P_2O_5 = 0.24, H_2O = 0.20) with an FMQ buffer (Dauphas et al., 2014). The circles in the background correspond to $\delta^{57}Fe$ from the literature (Foden et al., 2015; Poitrasson and Freydier, 2005; Schuessler et al., 2009; Sossi et al., 2012; Telus et al., 2012; Teng et al., 2013; Williams et al., 2018; Zambardi et al., 2014; Du et al., 2017; He et al., 2017; Xia et al., 2017*).*

Highlights:

- This DFT-based study provides new and self-consistent Fe and Si isotope fractionation factors for the main magmatic minerals present in the crust.
- Iron isotope fractionation factors between Fe^{2+}-bearing minerals are not negligible even at magmatic temperatures.
- For a given temperature and oxidation state, the local cationic environment of Fe or Si is the main factor influencing the isotopic properties of silicate minerals.
- Fractional crystallization is a viable way to explain the heavy iron isotope signature of the most evolved lavas.